UNIVERSITÄT MÜNSTER

BACHELOR THESIS

Studies on the Temperature Characteristics of the Detection Efficiency of Hamamatsu R15458-02-Type Photomultipliers

Supervisor:
Prof. Dr. Alexander KAPPES

Second examinor:
Dr. Volker HANNEN

A thesis submitted in the fulfillment of the requirements for the degree of Bachelor of Science

by

Frederick KRAFFT

AG Kappes
Institute Of Nuclear Physics
Department of Physics

October 4, 2024

Contents

1 Introduction

For centuries, the night sky has captivated observers, inspiring questions that have driven the progress of science. Over time, our understanding of the surrounding universe and its history has grown, driven by advancements in technology and theory. In the early 17th century, prominent minds like Galileo Galilei were the first to observe celestial objects with optical telescopes, revealing an unseen view on the planets and moons surrounding us. Over the subsequent centuries, humanity constructed a variety of telescopes, advancing into more and more distant parts of the universe - also into those that are hidden to the human eye. In recent decades, beyond electromagnetic radiation, astronomers have aimed to detect new types of *messengers* of the universe, such as gravitational waves, cosmic rays, and *neutrinos*, thereby broadening the observable spectrum of information.

Uncharged and nearly massless: Due to their unique nature, neutrinos exclusively interact with matter via the weak interaction and, although extremely weak as a result of their low mass, gravity. This property makes them particularly undisturbed cosmic wanderers, carrying nearly undistorted information about their origin. However, likewise this makes their detection a difficult task. The *IceCube Neutrino Observatory* tackles this challenge by instrumenting a large volume of Antarctic deep ice [1]. If a high-energy neutrino interacts with the ice, it produces secondary particles, emitting Cherenkov-light, which is then detected by digital optical modules (DOMs), populating the detector's volume [1]. The modules are equipped with photomultiplier tubes (PMTs), which are extremely sensitive photodetectors, allowing for the detection of individual photons. To allow correct interpretation of the recorded events, it is crucial to study the PMTs sensitivity precisely. The detection efficiency (DE) is of particular interest, characterizing the PMT in terms of the fraction of photons striking the photocathode and those that are ultimately detected as a measurable signal. The DE is highly dependent on the wavelength of the incident light, but is also a temperature dependent parameter. Since the operation temperatures of the PMTs for IceCube vary as a function of deployment depth, it is necessary to look into the temperature dependence of the properties of the PMTs, including sensitivity parameters as the detection efficiency.

Within the framework of this thesis, the detection efficiency of the R15458-02 PMT by Hamamatsu was studied for a range of wavelengths across the visible spectrum as a function of temperature, reaching from room temperature down to $-40\,^\circ$C. The new PMTs will find their place in the multi-PMT Digital Optical Modules (mDOMs), which are part of IceCube's extension *IceCube Upgrade*, aiming to increase the detector's sensitivity for lower energies in the order of several GeV significantly, expanding the horizons in the event reconstruction, particularly for neutrino oscillations. After a brief introduction on the physics behind IceCube's neutrino detection in chapter 2 and a more detailed insight into the operation of PMTs in chapter 3, chapter 4 presents a detailed description and discussion of experimental studies on the temperature dependence of the mDOM PMTs detection efficiency.

2 Neutrino Astronomy with IceCube

After AMANDA (**A**ntarctic **M**uon **a**nd **N**eutrino **D**etector Array) [2] demonstrated that the deep Antarctic ice is suitable for detecting high energy neutrinos in the mid 1990s, IceCube's neutrino detector was constructed on the same spot near the Amundsen-Scott South Pole Station as the first cubic kilometer scale detector worldwide [1]. As illustrated in fig. 2.0.1, 86 strings of Digital Optical Modules (DOMs) are deployed in at a depth of $1450\,\text{m}$ - $2450\,\text{m}$ in a hexagonal grid with a spacing of $125\,\text{m}$ [1]. Each string holds 60 DOMs, resulting in a total of 5160 modules distributed over the instrumented volume. One DOM contains a single photomultiplier tube with a diameter of $24\,\text{cm}$ encapsulated in a pressure vessel. The vertical spacing of the modules is $17\,\text{m}$ for the main detector, while in the center a more densely instrumented extension named *DeepCore* is embedded at depths ranging from $2100\,\text{m}$ - $2450\,\text{m}$ with a vertical distance of $7\,\text{m}$ [1]. A denser instrumentation of the volume results in a shorter path for the photons emitted by the charged secondary particles to reach a sensor. The shorter path goes with a reduction of absorption and scattering of the photons before detection. The denser mesh provides a higher resolution of the directional and positional information and, generally speaking, a higher probability density of detection. The recorded neutrinos have energies between $10\,\text{GeV}$ and $10\,\text{PeV}$ [3]. The lower energy neutrino observations in the $10\,\text{GeV}$ - $100\,\text{GeV}$ range rely on DeepCore [3]. Given the importance of instrumentation density for detecting low-energy neutrinos, IceCube is scheduled for an extension, known as *IceCube Upgrade*, which will feature a denser array, enhancing sensitivity to low-energy
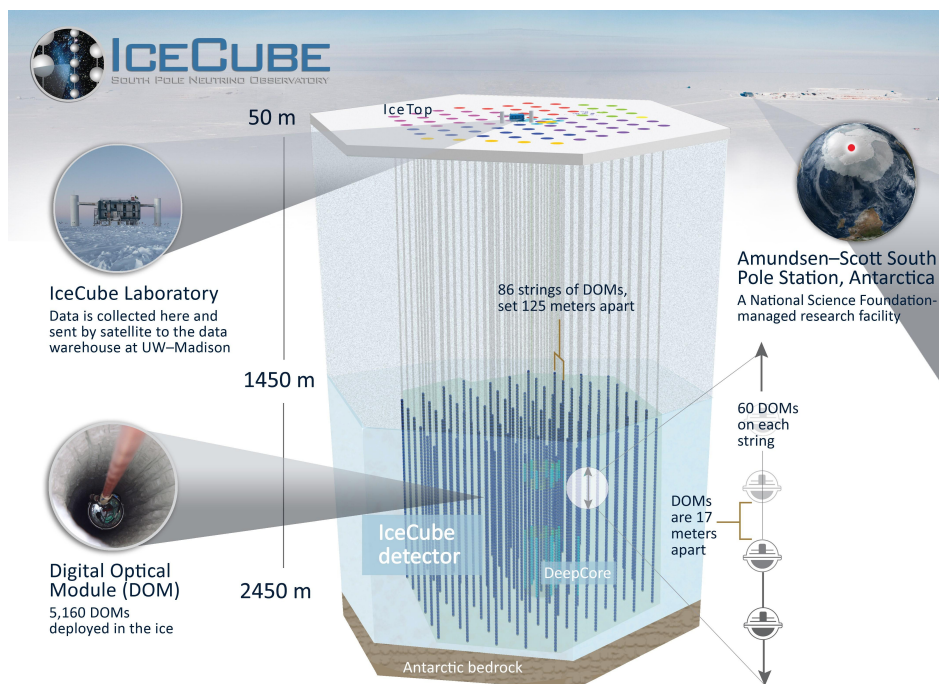

FIGURE 2.0.1: Schematic visualization of the IceCube Neutrino Observatory. Taken from [1].

events of under $\sim 10\,\text{GeV}$ [4]. The thick layer of arctic ice down to $1450\,\text{m}$ shields the detector from a significant fraction of potential background radiation, such as atmospheric muons produced as the result of interactions between cosmic rays and the Earth's atmosphere. However, high energy muons (above $\sim 1\,\text{TeV}$) can travel several kilometers through the ice and therefore constitute a significant background source for IceCube. The surface array IceTop consists of 81 stations, each of which containing a downward facing PMT, measuring charged particles from cosmic ray showers in the energy range of $10 \times 10^{14}\,\text{eV}$ - $10 \times 10^{18}\,\text{eV}$ [5]. This plays a crucial role in filtering a large portion of atmospheric muons as well as some atmospheric neutrinos detected by the in-ice detector which are on coincidence with atmospheric muons. Aside, analyzing the combined events registered by the in-ice and the surface detector makes IceCube a unique facility for studying cosmic ray physics, for more detail refer to [5]. Due to the exceptional capabilities of IceCube, especially in the detection of high-energy muons and neutrinos, the observatory plays a significant role in contemporary multi-messenger astronomy. In this field, information carried by several *messengers*, such as electromagnetic radiation, cosmic rays, gravitational waves, and neutrinos originating from a common extraterrestrial source are collected by multiple observatories around the world. IceCube participates in collaborations like the SNEWS network (Supernova Early Warning System) or the GCN (Gamma-ray Coordinates Network), aiming to extend the spectrum of sources of information for extraterrestrial events [3]. The underlying physical phenomena on which large-volume detectors like IceCube's are based on will be discussed briefly in the following. Furthermore, to embed this thesis in its context, IceCube's plans to enhance the detector with *IceCube Upgrade* will be outlined in section 2.3.

2.1 High-Energy Neutrino-Interaction with Matter

Neutrinos are elementary particles which are represented in the standard model in the form of three flavors, being the electron-, muon- and tauon neutrino. Neutrinos are leptons and therefore each have antiparticles with the opposite lepton number. Since neutrinos have no charge, they do not interact electromagnetically. Additionally, their minimal mass results in their gravitational interactions being exceptionally weak. Thus, neutrinos are most recognizable in weak interactions, which also led to their postulation in 1930 by Wolfgang Pauli, who was puzzled about the continuous energy spectrum of beta decay [6].

High-energy neutrinos with energies in the $20\,\text{GeV}$ - $500\,\text{GeV}$ range interact mainly by deep inelastic scattering on nucleons, as they have enough energy to resolve the inner structure of the target [7, p. 36-38]. The development of large-volume neutrino detectors like IceCube demonstrated, that this is also the predominant interaction form for higher energy neutrinos in the TeV scale [8]. The scattering processes with neutrinos take place with the exchange of a $W^{\pm}$- or a Z-boson and are then referred to as a *charged current* or *neutral current* interaction, respectively. In the case of deep inelastic scattering, the interaction can be described as follows:

$$\overset{(-)}{\nu_l} + N \xrightarrow{W^{\pm}} \overset{(-)}{l} + X, \quad \overset{(-)}{\nu_l} + N \xrightarrow{Z} \overset{(-)}{\nu_l} + X$$

As indicated in the above equation, the high energy neutrino ν_l with an arbitrary lepton flavor $l = e, \mu, \tau$ scatters off the nucleon N with either charged current interaction (l.h.s) or neutral current interaction (r.h.s). Both interactions lead to the creation of a hadronic shower (X) and to the production of a lepton l for charged current, or of a corresponding lepton-neutrino ν_l for neutral current, respectively. The interactions proceed analogously for antineutrinos, as indicated by the bracketed bars in the interaction equation above.

2.2 Cherenkov Radiation & Neutrino Detection

As explained in section 2.1, high-energy neutrinos interact by scattering off nucleons, whereby a fraction of their energy is transferred to secondary particles. If the nucleons are components of a dielectric medium, the charged secondary particles briefly polarize the atoms in their trajectory as they pass through the medium with velocity v_p. The atoms along the trajectory then emit spherical electromagnetic waves. If the particle travels slower than the speed of light in the medium $c' = c/n$, where c is the speed of light in vacuum and n is the refractive index of the medium, the spherical waves cancel each other out. However, if $v_p > c'$, the adjacent spherical waves do not cancel each other completely, leading to the formation of a conical wavefront traveling at velocity v_w along the path. First experimentally demonstrated by Pavel Cherenkov in 1934, this effect is now known as *Cherenkov radiation* [9].

The conical wavefront can be characterized in terms of its opening angle θ to the trajectory of the particle, depending on the velocity of the generated wavefront $v_w = c/n$, where c is the speed of light in vacuum and n is the refractive index of the medium, and the velocity of the charged particle v_p. As illustrated in fig. 2.2.1, it follows for the angle θ with $\beta = v_p/c$ that

$$\cos\theta = \frac{v_w t}{v_p t} = \frac{1}{\beta n}.$$

FIGURE 2.2.1: Schematic of the formation of the conical wave front of Cherenkov radiation, with the velocity v_w when a charged particle passes through, with the velocity v_p in a time interval t. Taken from [10, p. 16].

Due to the high energies necessary to produce Cherenkov radiation, the wavelength of Cherenkov light is typically in the blue end of the visible, or in the UV range for common dielectric transparent media like ice or water [9]. As the interaction probabilities of neutrinos are extremely low, it is a challenging task to find and construct transparent dielectric detectors, which provide a sufficient interaction probability for neutrino astronomy. As the interaction probability increases with the size and density of the detector, aside from building cost-intensive artificial detectors, water and ice are the predominant candidates for neutrino detector media. Arctic deep ice proofed its unique optical properties for neutrino detection, being exceptionally consistent due to the solid structure, during the AMANDA project [1]. Nevertheless, a significant amount of dust and bubbles is encapsulated in the ice, resulting in scattering effects of the wavefront. The inhomogeneous impurities make it necessary to characterize the propagation effects precisely by quantifying parameters like the average distance to absorption and the average distance between successive scattering of photons [11]. For IceCube, the parameters were experimentally determined by using LED light flashers on board of the modules [11].
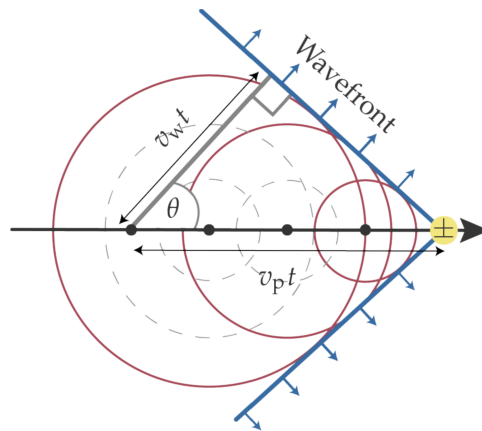
2.3 IceCube Upgrade

After more than a decade of research, IceCube gained a deep understanding of the capabilities of the detector. A shortage of statistics, coupled with the need for improved event reconstruction techniques, particularly at lower energies, represents a significant obstacle to

achieving IceCube's ambitious neutrino astronomy goals, such as accurately identifying extraterrestrial neutrino sources. Aware of the potential of a denser, more sensitive detector for low-energy event reconstructions in the order of several GeV, IceCube strives to extend the instrumentation of the ice in depths between $2150\,\mathrm{m}$ - $2425\,\mathrm{m}$, referred to as the physics region, which boasts the highest optical clarity and low atmospheric muon background [4].

The new strings will be densely packed with approximately 700 advanced optical modules, besides others featuring the *multi-PMT Digital Optical Module* (mDOM) [4]. The placement and configuration of the strings compared to the existing detector structure are indicated in fig. 2.3.2. One mDOM contains 24 PMTs with a diameter of $80\,\mathrm{mm}$ each [13], evenly distributed under the pressure vessel of the module, as shown in fig. 2.3.1. This poses a sensitive area which aims to be distributed homogeneously in all directions, maximizing the amount of directional information, opening up new possibilities in the reconstruction of events and

FIGURE 2.3.1: Photo of a Prototype of an mDOM, one of the IceCube Upgrade's new optical modules. Taken from [12].

background suppression [13]. The PMT used for the mDOM is the R15458-20 developed by Hamamatsu, where the suffix "-20" specifies that a base is included [13]. The PMT model R15458-02, which comes without a preattached base by the manufacturer, will be examined specifically in this thesis. The operating temperatures for IceCube's modules vary as a function of depth, as studied for the boreholes of the AMANDA project in [14]. According to their measurements, temperatures for the depths of *DeepCore* ($2100\,\mathrm{m}$ - $2450\,\mathrm{m}$) may range from $\sim -30\,^\circ\mathrm{C}$ up to $\sim -20\,^\circ\mathrm{C}$.
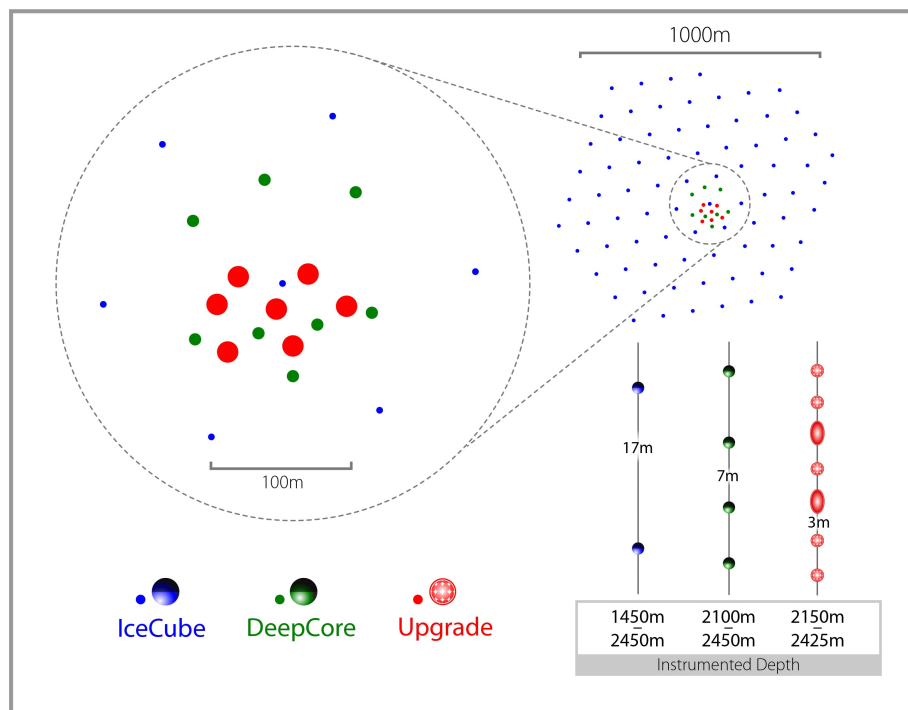

FIGURE 2.3.2: Schematic of the string positioning of the IceCube Upgrade project. The seven new strings (red) will be embedded in *DeepCore*. Taken from [12]

3 Photomultiplier Tubes

Photomultiplier tubes (PMTs) are light-sensitive devices engineered to detect very faint light signals, including those at the single-photon level. Characterizing their properties is essential for correctly interpreting the measured signal. Section 3.1 briefly outlines the working principle of a PMT, while introducing essential parameters that characterize the PMT in operation. In particular, the detection efficiency as the central parameter of this thesis will be introduced in more detail in a designated section 3.2. Subsequently, in section 3.3 and section 3.4, the PMT response and the methods to process it correctly are outlined.

3.1   Structure and Operating Principle

A photomultiplier tube is an evacuated glass tube, which envelops an inner structure that consists of a photocathode and a system of electrodes. The photocathode of a PMT is commonly a thin layer of a specific semiconductor that can convert light into electrons, based on the *photoelectric effect*. The functionality of a PMT is to multiply the photoelectron to obtain a measurable electric signal. As visualized in figure 3.1.1, the emitted photoelectrons (blue) are accelerated towards the multiplication system, which is at a higher potential than the photocathode. Additionally, focusing electrodes optimize the shape of the electric field, so that photoelectrons are guided into the multiplication system with the best possible efficiency. The multiplication system typically consists of 6 to 14 dynode stages [15, p. 203], which are electrodes at which successively higher potentials are applied. When the photoelectron strikes the first dynode, secondary electrons (yellow) are emitted, which are consequently accelerated to the next dynode, where again secondary electrons are emitted, increasing the

FIGURE 3.1.1: Schematic visualization of the photon detection principle of a PMT. The photocathode emits a single photoelectron (blue line) as a consequence of an incident photon, represented by the red sinodial line. When the photoelectron reaches the first dynode, secondary electrons (yellow) are emitted. Taken from [10, p. 37].

total number of electrons. The average total multiplication factor of the dynode system is referred to as the **gain**. At the end of the multiplication system, the electrons reach an anode, at which the output signal can be measured.
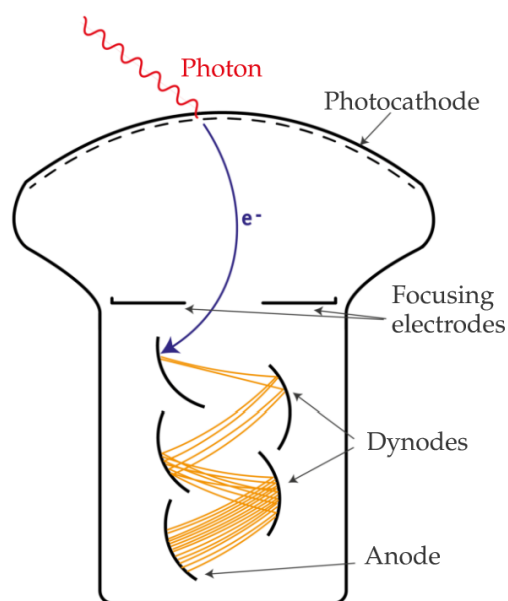
3.1.1 Photocathode

The photocathode is a thin vapour-deposited semiconducting layer on the inside of the entry window. For the majority of PMT applications in research and industry, the cathodes consist of one of three types: bialkali (K_2CsSb), rubidium bialkali (Rb_2CsSb), and S20 (Na_2KSbCs) [15, p. 50]. The choice of the cathode material and its fabrication parameters, as the ratio between the alkali compounds or the temperature at which the vapour-deposition is conducted, enables to fit the sensitivity of the photocathode to a defined spectrum. To characterize the photocathode's sensitivity in dependence of the wavelength λ of the incident light with the radiant flux ϕ, it is useful to introduce an efficiency parameter. The conversion fraction of photons that emit a photoelectron is referred to as the so-called **quantum efficiency** (QE). Noting $n_e = I/e$ is the total number of photoelectrons, described by the fraction of the photocathode current I and the elementary charge e and that the number of incident photons is given by $N = \phi/E_\lambda$, with the photon energy $E_\lambda = h \cdot c/\lambda$, the fraction can be expressed as

$$QE(\lambda) = \frac{n_e}{N} = \frac{I/e}{\phi/E_\lambda}. \tag{3.1.1}$$

For the bialkali photocathodes of the mDOM PMT, the quantum efficiency peaks for wavelengths in the UV-region to the lower end of the visible spectrum [10, p. 69], which is optimal for the dominant wavelengths of the produced Cherenkov light by neutrino events (see section 2.2). The energy of the released photoelectron E_{pe} is also highly wavelength and material dependent, which manifests in the expression

$$E_{pe} = E_\lambda - W, \tag{3.1.2}$$

where W is the specific work function of photocathode surface material, as postulated by Albert Einstein in 1905 [16, p. 145-148]. The equation also implies the existence of a cut-off wavelength λ_0, for which $E_\lambda < W$, meaning that the incident photon does not have the sufficient energy to excite an electron from the valence to the conduction band. The energy of the photoelectron influences the time between the incidence of the photon and the response of the anode, since it determines the initial momentum in the acceleration process to the first dynode.

3.1.2 Collection and Multiplication System

As the potential differences and distances of the dynode stages are fine-tuned precisely to guide the secondary electrons through the dynode stages, each dynode multiplies the primary electrons N_{in} on average by a specific factor, referred to as the stage gain δ. Thus, the average number of secondary electrons for a dynode stage is given by $N_{out} = \delta \cdot N_{in}$. In [15, p. 205] a semi-empirical formula is proposed, which describes a linear behavior between inter-dynode voltage ν and the number of released secondaries N_{out}, while accounting for scattering losses with an index $\beta < 1$ for ν:

$$\delta = \frac{N_{out}}{N_{in}} = \alpha \cdot \nu^\beta, \tag{3.1.3}$$

where α describes the proportionality of voltage and the stage gain without scattering losses. The overall gain of the dynode system consisting of N dynode stages finally can be expressed as the product of the stage gains

$$G = \prod_{i=1}^{N} \delta_i = \prod_{i=1}^{N} \alpha_i \cdot \nu_i^{\beta_i}. \tag{3.1.4}$$

The total gain is finally determined by the total operating voltage V, which is applied to the base of the PMT. A voltage divider distributes the voltage to the dynodes, so that $V = \nu_1 + \nu_2 + \cdots + \nu_N$. Thus, it follows for the gain G, that

$$G = a \cdot V^b, \tag{3.1.5}$$

where $a = \alpha_1 \cdot \alpha_1 \cdot \ldots \cdot \alpha_N$ and $b = \beta_1 + \beta_2 + \cdots + \beta_N$. In most applications, the voltage is applied, so that the resulting gain is in the order of $\mathcal{O}(10^4) - \mathcal{O}(10^8)$ [15, p. 204], depending on the PMT model and application purpose. The chosen gain and corresponding voltage for operation are referred to as the *nominal gain* and the *nominal voltage*, respectively.

Even though the focusing electrodes improve the electric field between the photocathode and the first dynode, not all photoelectrons reach the first dynode stage ultimatly. Likewise, a fair number of secondary electrons are being *lost* in the multiplication system. Thus, it is necessary to define the **collection efficiency** F of a PMT, as the ratio of photoelectrons that lead to a measurable signal at the anode and the total number of photoelectrons emitted from the photocathode. Since losses on higher stages only reduce the total gain, rather than the collection efficiency, the collection efficiency is predominantly determined by the probability of a photoelectron reaching the first dynode stage.

In an idealized PMT, the collection efficiency is 100%, meaning that the idealized gain G_{ideal} would be the direct ratio between the anode current I_a and the photocathode current I_{pc}, thus $G_{\text{ideal}} = I_a/I_{\text{pc}} = 1$. Hence, the collection efficiency can be expressed as the ratio of the ideal and the actual gain

$$F = \frac{G}{G_{\text{ideal}}}. \tag{3.1.6}$$

The real gain can be obtained by fitting the charge spectrum of the PMT response for single photoelectrons, which will be discussed in 3.4.

3.2 Detection Efficiency

Based on the definitions from the previous section 3.1.2, the total ratio of the photons striking the photocathode N_λ and those that can ultimately be detected as a measurable signal n_λ are defined as the **detection efficiency** $\text{DE}(\lambda)$ and can be expressed as the product of the collection efficiency $F(\lambda)$ and the quantum efficiency $\text{QE}(\lambda)$

$$\text{DE}(\lambda) = F(\lambda) \cdot \text{QE}(\lambda) = \frac{n_\lambda}{N_\lambda}. \tag{3.2.1}$$

The average number of detected photons can be approximated by

$$n_\lambda \approx \frac{\langle Q \rangle}{G_\lambda \cdot e} \tag{3.2.2}$$

where $\langle Q \rangle$ is the mean charge of the measured PMT responses and G_λ is the gain of the PMT. Since a mean value is considered, the equation only holds for a statistically sufficiently large number of measured waveforms.

Apart from the spectral dependence of the detection efficiency, due to the material-characteristics of the individual components of the PMT, in particular the photocathode, the DE is also dependent on the operation temperature. Expediently, it is reasonable to introduce a coefficient which describes the change of the detection efficiency with temperature as a function of the wavelength. In this thesis, $\alpha_{\text{DE}}(\lambda)$ as the normalized temperature dependence coefficient for the detection efficiency is obtained by fitting the slope of $\text{DE}_\lambda(T)/\text{DE}_{\lambda,\text{room}}(T)$ as a function

of temperature T for each wavelength, individually:

$$\frac{\text{DE}_\lambda(T)}{\text{DE}_{\lambda,\text{room}}(T)} = \alpha_{\text{DE,fit}}(\lambda) \cdot (T - T_R) + 1 \qquad (3.2.3)$$

$\text{DE}_{\text{room}}(\lambda)$ denotes the detection efficiency at room temperature $T_R = 20\,°\text{C}$. Similary, a absolute temperature dependence coefficient $\beta_{\text{DE}}(\lambda)$ is introduced as

$$\text{DE}_\lambda(T) = \beta_{\text{DE,fit}}(\lambda) \cdot T + c_\lambda, \qquad (3.2.4)$$

which helps to compare, which temperature sensitive spectral ranges described by $\alpha_{\text{DE}}(\lambda)$ actually lead to a relevant in- or decrease in DE. For example, if the detection efficiency is very low, a relatively small temperature dependence can result in a large $\alpha_{\text{DE}}(\lambda)$, while the absolute in- or decrease of DE is rather small, reflected in a small $\beta\text{DE, fit}(\lambda)$.

The temperature dependence of DE is anticipated to be predominantly influenced by the photocathode material's temperature dependence, reflected in the QE contribution. The collection efficiency F represents the likelihood of a released photoelectron reaching the first dynode to initiate the multiplication process. Consequently, the temperature-dependence of F is primarily determined by the properties of the first dynode's material. Since a reduction in the stage gain of the first dynode affects only the total gain, as long as a multiplication process is initiated, F remains mostly unaffected by temperatures, as also demonstrated experimentally in [17].

3.3 Operation Modes and Timing Parameters

Depending on the scope of the measurement, the anode signal can be measured as a voltage drop or a charge, that built up over a defined time window. Measuring the voltage signal is referred to as **pulse-mode**. In pulse mode, the anode signal is connected to a resistor. Thus, at sufficiently low photon rates, the resulting voltage drop can be assigned to the detection of a single photoelectron. The voltage drop can be measured with an oscilloscope in high resolution, revealing response distributions of the PMT, often referred to as waveforms. The integration of the waveforms delivers the charge. Based on the charge, the waveform can be traced back to the number of measured pho-
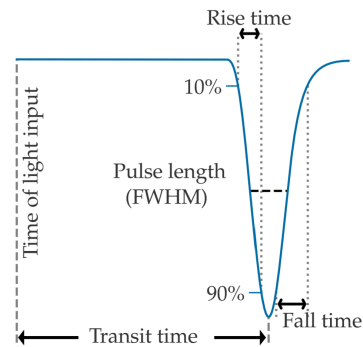

FIGURE 3.3.1: Schematic of the timing and shape parameters that describe a PMT response pulse. Taken from [10, p. 38]

toelectrons. The characteristic timing parameters of the PMT response are visualized in figure 3.3.1.

The **transit time** is the total time between the incidence of the photon at the photocathode and the response of the anode. Due to the slight variations of the paths of the electrons, the timing of the response can vary. The distribution around the mean transit time is usually characterized by defining a **transit time spread** (TTS) as the standard deviation. Additionally, the rise- and fall-time of the pulse are usually defined as the time intervals from $10\% - 90\%$ of the amplitude of the pulse, respectively before and after the maximum, as shown in figure

3.3.1. In general, the rise- and fall time are not equal. However, at higher photon rates, the response distributions of the PMT may overlap. If the responses overlap in an interval smaller than the TTS, the response cannot be distinguished, posing a minimal limit for the time resolution of the PMT. The alternative to pulse mode is operating the PMT in **current mode**, where the signal is directly integrated within in a defined time window using a picoammeter.

3.4 Charge Spectrum

Anticipating the transit time of photoelectrons potentially emitted as a consequence of a light pulse, a time window of the expected response can be defined, in which the charge of the pulse is obtained by integration, as shown in fig. 3.4.1. Thus, if no photon is detected in the interval, only the baseline and noise is integrated, which results in a sharp Gaussian distribution located around a charge close to zero in the charge histogram 3.4.1, which is commonly denoted as the pedestal. The detection of a single photoelectron results in a distribution $S_1(q)$, as indicated in figure 3.4.1. The mean charge of the distribution $S_1(q)$ is $G \cdot e$ as the mean number of secondary electrons produced if a photoelectron reaches the multiplication system. If n photons are detected in the same pulse, the obtained voltage drop corresponds to the total charge of the sum of all photoelectrons, accordingly. Hence, the distribution of the charge is the convolution of n SPE distributions that can be expressed by:
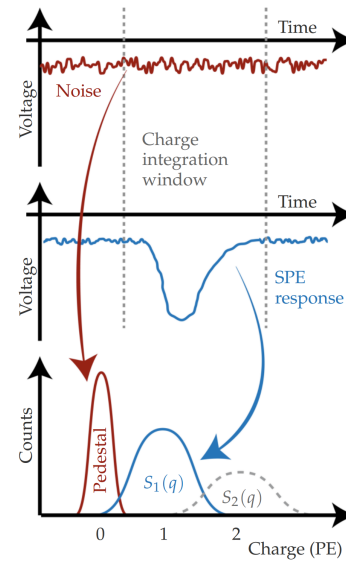

FIGURE 3.4.1: Schematic of the charge integration of a PMT response, obtaining the SPE distribution. Taken from [10, p. 44]

$$S_n(q) = S_1(q) * S_{n-1}(q) \tag{3.4.1}$$

The total charge distribution of the PMT response is the convolution of the pedestal, as well as other background effects as the dark rate and under-amplified pulses, the SPE response $S_1(q)$ and the contribution defined by the mean number of electrons N that are emitted per waveform. The latter can be modelled by a Poisson distribution

$$P(N, \mu) = \frac{\mu^N e^{-\mu}}{N!} \tag{3.4.2}$$

for a typical light source as a LED or laser and depends on the mean number of photoelectrons reaching the multiplication system μ [18, p. 50]. The mean number of photoelectrons reaching the multiplication system is given by the mean number of incident photons per pulse n_γ, intrinsically reduced by the quantum efficiency of the photocathode QE_λ and the collection efficiency F of the PMT:

$$\mu = n_\gamma \cdot \mathrm{QE}_\lambda \cdot F. \tag{3.4.3}$$

The distribution for the charge of n photoelectrons can be approximated by a Gaussian distribution around its mean Q_n with the standard deviation σ_n [10, p. 45]:

$$G(q, Q_n, \sigma_n) = \frac{1}{\sqrt{2\pi}\sigma_n} \exp -\frac{(q - Q_n)^2}{2\sigma_n^2}. \tag{3.4.4}$$

Assuming that the amplification processes for multiple photoelectrons per pulse can be considered independent, by folding 3.4.4 and 3.4.2 the ideal SPE response is obtained as

$$S_{\text{ideal}}(q) = \sum_{n=0}^{\infty} \frac{\mu^N e^{-\mu}}{N!} \cdot \frac{1}{\sqrt{2\pi}\sigma} \exp\left(-\frac{(q - Q_n)^2}{2\sigma^2}\right) \tag{3.4.5}$$

which, however, does not describe the real response distorted by the background effects. Modeling the background requires an extensive parametrization of background contributions, which is discussed in [19] in full detail. Defining a probability to measure a charge distribution from background effects allows establishing a probability density function of the charge distribution, separated into Gaussian contributions for the photoelectrons with the probability $1 - P_u$ and the background-induced non-Gaussian contributions with the probability P_u. As concluded in [10], the probability density function can be modelled by

$$f(q) = \sum_{n=0}^{\infty} \frac{\mu^N e^{-\mu}}{N!} \Big[(1 - P_u) \cdot G(q, Q_n, \sigma_n)$$
$$+ P_u \cdot \frac{\lambda}{2} \cdot e^{-\lambda \cdot (q - Q_n - \frac{1}{2}\lambda n\sigma_1^2)} \cdot \text{erf}\left(\frac{Q_n - q + \lambda n\sigma_1^2}{\sqrt{2n}\sigma_1}\right) \Big], \tag{3.4.6}$$

where $Q_n = Q_0 + n \cdot Q_1$ and $\sigma_n = \sqrt{\sigma_0^2 + n\sigma_1^2}$ with the mean Q_0 and width σ_0 of the pedestal. Equation 3.4.6 allows fitting the charge distribution of the PMT, which will be used to determine the gain $G = Q_1/e$ of the PMT by division of the elementary charge e in the framework of this thesis.

4 Detection Efficiency of Hamamatsu R15458-02-Type PMTs

As explained in section 2.3, the in-ice operating temperatures for the mDOM are expected to range from $-20\,°\mathrm{C}$ to $-30\,°\mathrm{C}$, which potentially impacts the sensitivity of the PMT. The focus of this thesis will be on the detection efficiency as the total probability of a photon being detected by a PMT, which is a highly wavelength-dependent parameter. All conducted experiments are build around the same R15458-02-type PMT[1] by Hamamatsu. To compare the characteristics to those under room temperature, in the framework of this thesis the PMT was cooled down from room temperature to $-40\,°\mathrm{C}$, stepwise, under variation of the wavelength across the visible spectrum (VIS) between $460\,\mathrm{nm}$ - $650\,\mathrm{nm}$ for each temperature step. It was also attempted to repeat the measurements for the ultraviolet spectrum (UV) between $350\,\mathrm{nm}$ - $480\,\mathrm{nm}$, which ultimately did not produce significant result as it was distorted by systematic errors, due to changes in the setup. Due to time constraints, the methods could not be corrected. The difficulties and partially solution approaches for the investigation of the DE in the UV-spectrum are discussed in section 4.2.4.

To test the experimental methods in a simplified environment, a pre-stage setup was designed, presented in section 4.1. In this setup, temperature and wavelength are fixed at room temperature and a constant spectrum peaking at $459\,\mathrm{nm}$ respectively. The main objective of this setup is to ensure that the experimental methods to determine the detection efficiency (DE) with eq. (3.2.2) are valid for a region of light intensity. This is crucial, since the intensity will vary to a certain degree while setting up various wavelengths with a wavelength selector. The pre-stage setup was also used to conduct a gain calibration for the specific PMT used, which is presented in section 4.1.1.

Building on the validation of the methods from the pre-stage setup, the experimental methods to investigate the temperature dependence and the results are discussed in section 4.2. In the first subsection 4.2.1, the parametrization of the optical components is discussed exemplary for VIS, which is the basis for the calibration of the reference photodiode used to determine the incident photon flux at the photocathode. Subsequently, the determination of the gain of the PMT as a function of temperature and wavelength is presented in section 4.2.2 for UV and VIS, which is necessary to calculate the detection efficiency based on eq. (3.2.2). Finally, the results of the investigation of the temperature characteristics of the detection efficiency dependent on the wavelength of the incident light are discussed in section 4.2.3.

4.1 Testing the Detection Efficiency Measurement Methods

As it is desired to conduct the DE measurements for a range of wavelength-steps, with the use of a wavelength selector, inevitably, the selection comes with change in the intensity of light across the spectrum. To ensure that this change does not cause systematic error for the measurement of the DE, a tunable light source was used to vary the intensity across several orders

---

[1]Serial number *BA0784*

of magnitude. This way, critical limits can be identified under or above which the measured DE deviates significantly from the expected DE. Furthermore, to investigate the limits of the utilization of eq. (3.2.2), the results are compared to the mean number of photoelectrons reaching the multiplication system μ obtained by fitting the charge spectra with eq. (3.4.6), which is expected to be equivalent to eq. (3.2.2). To determine the nominal voltage, which is set in the high-voltage supply[2] (HV), a gain calibration was performed beforehand. The calibration method is discussed in the following section 4.1.1.

The setup used to study the influence of light intensity on the measurement method in pulse mode is schematically visualized in fig. 4.1.1. The used tunable light source is an LED[3], which emits a broad spectrum of light, peaking at $459\,\text{nm}$. The light is then guided into the light-tight enclosure with a fiber. To calculate the number of incident photons at the photocathode N_λ, a calibrated photodiode[4] (PHD), with known quantum efficiency for the peak wavelength of $66.85\,\%$ is used, which is connected to a picoammeter[5]. The reference measurement is realized, by moving the PHD into the beam path before and after the measurement of the PMT response with a stepper motor[6]. This way, the intensity of the light, which can change slightly during the measurement, can be interpolated for the timespan of the PMT measurement. As the aim is to investigate the PMT response down to below to the order of one photon per pulse, it is necessary to insert a neutral density filter[7] (ND) in front of the PMT, since these extremely low currents cannot be detected by the PHD. An optical density of 4.0 turned out to be suited for the desired intensities. To prevent systematic errors in the reference measurement, the profile of the beam was scanned before the measurements, by moving the PHD on the vertical plane stepwise, to ensure the correct position for the PHD, so that the whole beam profile is incident on the PHDs surface. For centering the beam on the photocathode of the PMT, it was sufficient to visually check the light spot on the PMT, as the beam width is much smaller than the photocathode's sensitive surface. Nevertheless, it is essential to hold the position constant over all DE measurements and generally as central as
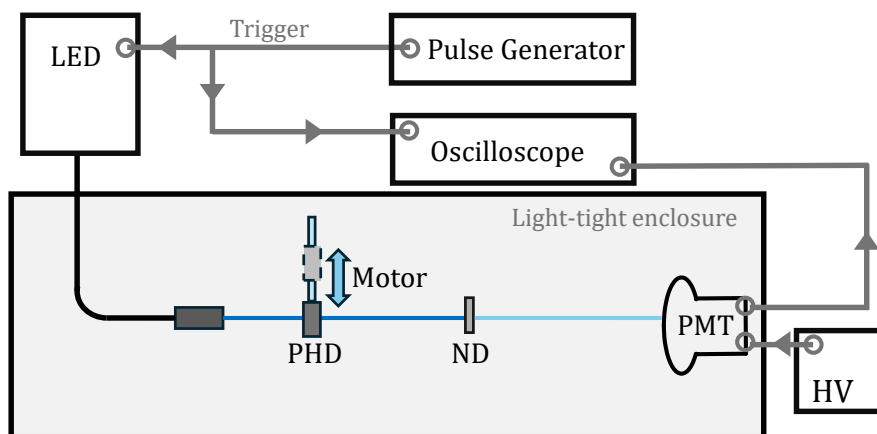

FIGURE 4.1.1: Experimental setup for the investigation of the dependence of the measurement method of the detection efficiency in pulse mode on the light intensity of the source. The photodiode (PHD) is connected to a picoammeter, which is not depicted here for the sake of overview.

---

[2]ECH244-type crate with EHS F4 40n HV-supply by iseg
[3]Model PDL 800-B by PicoQuant
[4]Model 818-UV/DB by Newport
[5]Keithley 6482
[6]Custom made: design and construction by Dipl. engineer Christian Huhmann
[7]ThorLabs NE50A-A Absorptive Neutral Density Filter (OD: 5.0)

possible, as the DE decreases approaching the outer rim of the PMT [10]. Another prepara-
tory measurement conducted, was the measurement of the transmittance of the ND-filter for
the specific spectrum of the LED (see section 4.1.2).

To minimize the background noise induced by unintended light sources in the laboratory, the
light sensitive instruments are enclosed in a light tight box, as shown in fig. 4.1.1. The fiber
and data-/high-voltage cables are guided out of the enclosure in photon mazes, again to avoid
background light in the enclosure. To align the PMT response to the light pulses, a pulse
generator[8] triggers light pulses in the LED at a fixed repetition rate, while simultaneously
providing the trigger for the oscilloscope[9]. The selection of the repetition rate was made,
trying to maximize the intensity without risking an overlap of the intended response pulses,
but also unintentional additional pulses produced by correlated background, as *afterpulsing*.
Afterpulses appear as the result of different effects. Some types of afterpulses appear sev-
eral microseconds after the regular pulse. The probability of the occurrence of afterpulses
are distributed over time, as each afterpulsing effect has its characteristic peaks in time. *Af-
terpulsing type II* (AP2) is one of the most relevant effects when selecting an upper limit
of the repetition rate, as it the probability of their occurrence peaks at $\sim 1\,\mu s$ and $\sim 3.2\,\mu s$
after the regular pulse [10, p. 122]. The probability of AP2 drops quickly after those peaks.
At $\sim 10\,\mu s$ the probability starts being negligible. Thus, $R = 100\,\mathrm{kHz}$ was chosen as the
repetition rate.

4.1.1 Gain Calibration

As discussed in section 3.4, the gain can be obtained fitting the SPE spectrum. To attenuate
the intensity of the LED, an absorptive neutral density was placed in the beam path. The
desired nominal gain of the PMT is chosen as $\sim 5 \times 10^6$. To determine the nominal volt-
age of the PMT, the applied voltage to the base is increased stepwise in steps of $25\,\mathrm{V}$ from
$900\,\mathrm{V}$ - $1380\,\mathrm{V}$, fitting the charge spectrum for each step. As an example, the left plot of
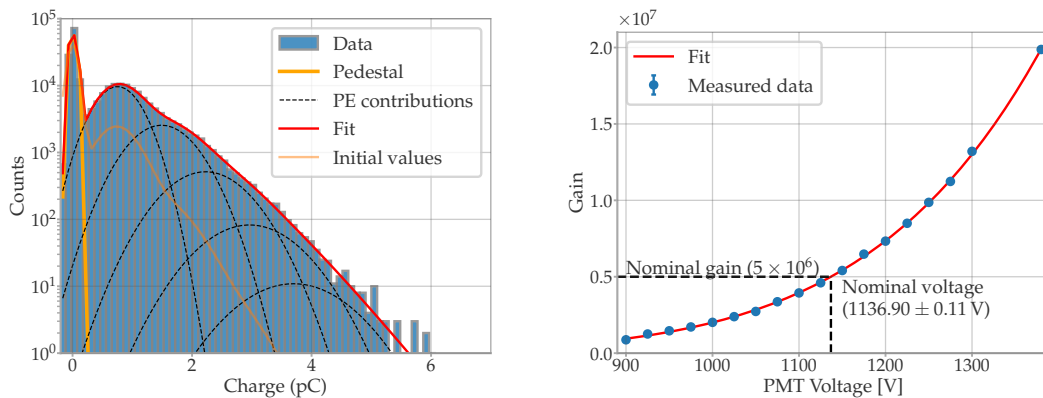fig. 4.1.2 shows the obtained charge distribution and fit for an applied voltage of $1125\,\mathrm{V}$. The

FIGURE 4.1.2: **Left:** Fit of the charge spectrum of the PMT for an applied total voltage of $1125\,\mathrm{V}$,
according to eq. (3.4.6). **Right:** Gain calibration for the PMT at room temperature. The voltage-gain
pairs are fitted with eq. (3.1.5). The fit parameters a and b are used to determine the nominal voltage
for a given nominal gain. The errorbars of the data points are smaller than the markers.

---

[8]Model DG1032 by Rigol
[9]PicoScope 6404C

fit of the charge spectrum considers the contributions belonging to the detection of n photo-electrons, described by Gaussian distributions with the mean Q_n, as described in eq. (3.4.4). From the mean Q_1 of the first PE contribution belonging to the detection of one photoelectron, the gain can be obtained as $G = Q_1/e$. Building on the fitted gain-voltage pairs, the pairs are fitted with eq. (3.1.5). Finally, rearranging the same equation and inserting the targeted nominal gain yields the nominal voltage. The application of the method is shown in the right subplot of fig. 4.1.2. Selecting a nominal gain of $G_n = 5 \times 10^6$, the corresponding nominal gain according to the fit parameters then is $U_n = 1136.90(11)\,\text{V}$ at room temperature. Due to an initial less-than-ideal fitting, an incorrect nominal voltage of $1131.9\,\text{V}$ was considered to correspond to a gain of 5×10^6 during the subsequent experiment. However, the use of slightly different voltage just shifts the nominal gain to $G_n = 4.8454(33) \times 10^6$.

4.1.2 Impact of Light Intensity on the Determination of the DE

As the specific transmittance of the used ND-filter for light of the LED is not known, it was necessary to measure it first. The filter was inserted between the LED head and PHD, as close as possible whilst maintaining perpendicular alignment. This ensures the beam is incident about orthogonal to the ND-filter and the PHD. Subsequently, the measurement is repeated once without the ND-filter, to act as a reference. Thus, the transmittance of the ND-filter can be calculated as the ratio of the measured photocurrents, while subtracting the ambient light in the enclosure from the numerator and the denominator. In this manner, the measured transmittance of the ND-filter used, specific to the wavelength of the light source, is found to be $3.907\,104(33) \times 10^{-5}$. Knowing the transmittance of the ND-filter and the wavelength-specific quantum efficiency of the used diode $\text{QE}_{\text{PHD},\lambda}$, the photocurrent I_{ref} can be interpreted in absolute terms, rearranging eq. (3.1.1), multiplied by the transmittance of the ND-filter T_λ, so that the average number of photons reaching the photocathode per light pulse is

$$N_\lambda = \frac{T_\lambda \cdot \phi}{R} \quad \text{with} \quad \phi = \frac{I_{\text{ref}} - I_{\text{bg}}}{\text{QE}_{\text{PHD},\lambda} \cdot e}, \qquad (4.1.1)$$

where I_{bg} denotes the measured photocurrent from background light in the enclosure, R is the repetition rate of the light source and e is the elementary charge. To determine the detection efficiency according to eq. (3.2.1), either based on eq. (3.2.2) or the fitting the charge spectrum with eq. (3.4.6), obtaining μ is used, so either

$$n_\lambda = \frac{\langle Q \rangle - \langle Q_{bkc} \rangle}{G \cdot e} \quad \text{or} \quad n_\lambda = \mu. \qquad (4.1.2)$$

The left equation considers that the charge spectrum is shifted due to a shift of the baseline, also referred to as background current, which must be subtracted from the mean charge consequently. The charge spectra fitted are reliable if the PMTs are illuminated with relatively small numbers of ~ 0.01 - 3 photoelectrons reaching the multiplication

FIGURE 4.1.3: Comparison of the calculated number of detected photons n_λ using the mean charge method and the charge fit method. The uncertainties are smaller than the marker size used.

system per pulse (μ), for more detail, see appendix A.1. Since μ cannot be selected when varying the wavelength with the wavelength selector, it is necessary to validate that the
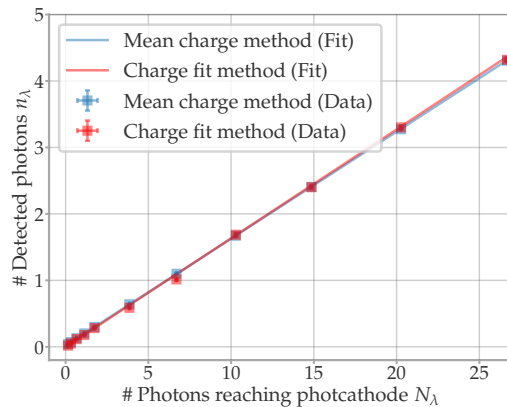
method that uses the mean charge produces the same results as using the fit parameters. Fig. 4.1.3 shows the direct comparison of the calculated number of detected photons n_λ with both methods for a number of set photons reaching the photocathode N_λ, calculated using eq. (4.1.1). As expected from eq. (3.2.1), the quantities show linear behavior, the slope being the detection efficiency. The obtained fitted detection efficiencies for both methods are

$$\mathrm{DE}_{\langle Q \rangle} = 16.102(55)\,\% \quad \text{and} \quad \mathrm{DE}_\mu = 16.38(29)\,\%. \tag{4.1.3}$$

Even though the result of the mean charge method $\mathrm{DE}_{\langle Q \rangle}$ is inside the confidence interval of DE_μ, it is misleading to assume, that both methods produce equivalent results considering their uncertainties. This becomes clearer, when comparing the detection efficiency resulting from both methods directly, as visualized in figure 4.1.4. The first thing that stands out is the significant increase in DE calculated with the mean charge method for low N_λ. An explanation for the systematic increase could be found in the subtraction of the baseline. Both baseline and response pulse are integrated using the *Simpson rule* over a fixed interval. Systematic errors in the selection of the time windows for both, would manifest in the resulting charge from the integration. While the time-window effects gets smaller when the measured charge of the pulses is much greater than the baseline, the effect gets more relevant for low intensities. As the intensity is reduced, the baseline is subtracted from itself more often per pulse. Therefore, the systematic error distorts the measured mean charges for $N_\lambda \to 0$. As can be seen on the magnified view on the right, the mean charge method seems to monotonously approaches the mean of both fitted detection efficiencies (4.1.3), which would indicate that the accuracy of the method rises for higher N_λ, as long the photocathode does not experience saturation, since higher intensities could decrease the systematic errors occurring while subtracting the baseline. For similar bialkali PMTs, linear behavior was observed for intensities under $\sim 300\,\mathrm{PE}$ emitted by the cathode, with a deviation of under $\sim 10\,\%$ [20]. Considering that the quantum efficiency of the specific PMT is below $\sim 30\,\%$ [10, p. 69] across all wavelengths, the corresponding upper limit for the number of photons reaching the photocathode can be approximated as ~ 1000 photons. Since the spectral QE vanishes for wavelengths approaching the red end of the visible spectrum, the limit could be set even higher, depending on the wavelength. Nevertheless, the intensity range for DE measurements was aimed at 10 - 1000 photons reaching the photocathode for successive experiments.
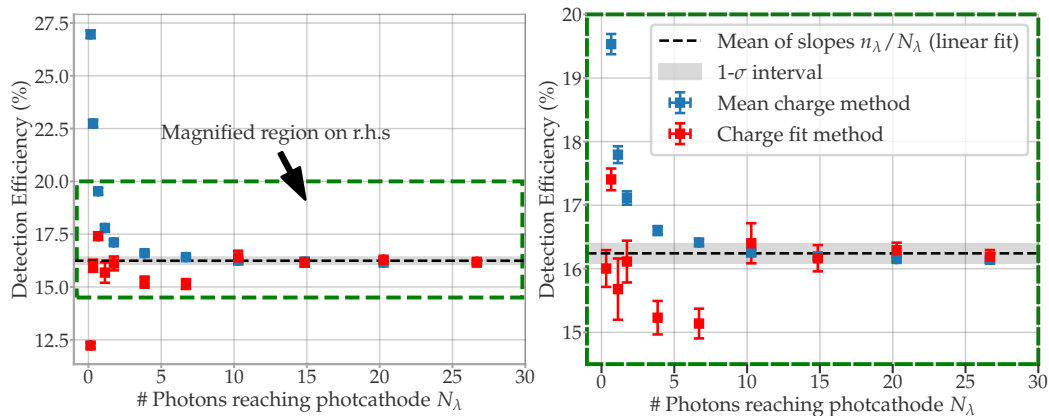

FIGURE 4.1.4: Resulting detection efficiencies obtained by using the mean charge and the charge fit method. The right-hand side shows the green marked region from the left-hand side compared to the mean of the fitted slopes of the n_λ/N_λ for both methods (4.1.3). Some uncertainties are smaller than the marker size. The legend holds for both subfigures.

4.2   Spectral Temperature Dependence of the Detection Efficiency

The experimental determination of the detection efficiency of a PMT requires simultaneous measurement of the photons reaching the photocathode N_λ and those that are detected by the PMT n_λ respectively (see eq. (3.2.1)). The measurement of the detection efficiency thus is built around the measurement of two main quantities for N_λ and, n_λ respectively:

1. The flux of the incident light ϕ_λ, which can be measured using a photodiode for reference.

2. The charge of the pulse Q, which is obtained by integration of the waveform of the PMT response, as shown in section 3.4.1.

As noted in equation 3.2.2, if the number of measured waveforms is sufficiently large, the mean charge of the response pulses divided by the gain of the PMT converges to the number of detected photons n_λ. Since the gain is both, a wavelength and a temperature dependent parameter, it was determined for the temperate-wavelength space in that the detection efficiency is aimed to be studied in. Based on the preparatory investigation on the influence of fluctuations in light intensities, the way is paved to use a wavelength filter, due to which the intensity of the light cannot be kept constant across the spectrum. The designed setup for the visible spectrum is visualized in fig. 4.2.1. Analogously to the previous setup from section 4.1, a pulsed light source[10] is synchronized with an oscilloscope [11], which receives the PMT signal simultaneously. The emitted light from the laser source is transmitted to the wavelength filter[12], where a desired wavelength is selected for transmission. Subsequently, the filtered beam is routed into a light tight enclosure. Entering the enclosure, the beam is divided into two separate beams with a beam splitter[13]. This allows guiding one part of the beam to a reference photodiode (PHD)[14] while obtaining a fraction of the beam to guide it to the PMT. The photodiode is connected to a picoammeter, which is not depicted for the sake of overview. The part of the beam guided in the direction of the PMT is attenuated by a combination of reflective neutral density (ND) filters[15][16], before it is transmitted into a
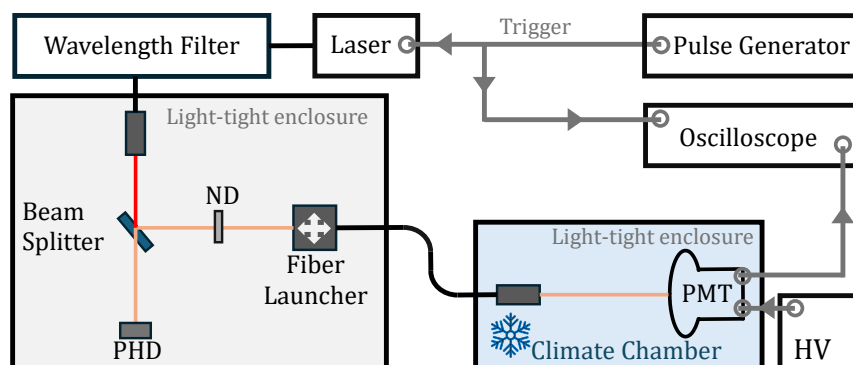

FIGURE 4.2.1: Experimental setup for the investigation of the temperature and wavelength characteristics of the detection efficiency in the visible spectrum. The photodiode (PHD) is connected to a picoammeter, which is not depicted here for the sake of overview.

---

[10]SuperK COMPACT by NKT Photonics
[11]PicoScope 6404C
[12]LLTF Contrast by NKT Photonics
[13]Model BSW20 by ThorLabs
[14]Model 818-UV/DB by Newport
[15]NDUV02A by Thorlabs
[16]NDUV03A by Thorlabs

fiber[17] using a fiber launcher[18]. The ND filters are selected, so that the number of incident photons on the photocathode are in the range between 10 - 1000 photons, as concluded in section 4.1. The fiber guides the remaining photons to the climate chamber[19]. To minimize the possibility of ambient light reaching the PMT, another light tight box is placed in the climate chamber, which contains the PMT. The voltage on the PMT base is held constant at the nominal voltage of 1132 V, with a high-voltage supply[20] (HV), calibrated with the previous setup (4.1.1). As the gain varies as a function of temperature and wavelength, setting the previously determined nominal voltage just ensures the desired order of the gain. The gain for each temperature-wavelength pair is measured separately, see section 4.2.2. With respect to previous studies on the temperature dependence of the quantum efficiency of the same PMT model ([21, 10]), it was decided to choose a resolution of 5 nm and 5 °C steps respectively, while leaving out the temperature step at 0 °C to minimize condensation effects and in general high humidity. Thus, at every incremental temperature between 20 °C and −40 °C, the spectrum ranging from 460 nm - 650 nm was repeatedly scanned. Considering that increasing the temperatures from cold to warm would cause defrost of ice in the climate chamber, the PMT is always cooled down from room temperature. In every cooling step, the temperature can settle for two hours before measurement, ensuring the PMTs temperature stabilizes at the set temperature.

To relate the light flux on the reference diode and the absolute number of incident photons on the PMT, a measurement of the ratio of the light intensity at the end of both beam paths is required. The results of the preparatory measurements concerning the optical setup are presented exemplary for the visible spectrum the in section 4.2.1. Aside from the optical parametrization, the transit time of the PMT was also determined as a function of wavelength, to potentially improve the setting of the charge integration window. However, the wavelength-dependence of the transit time proved to be negligible for the selection of the charge integration window (see appendix A.3).

The experimental setup for the investigations in UV (350 nm - 480 nm) only differs to the described setup for VIS in two aspects.

1. The wavelength filter is replaced with a tunable UV-extension[21]

2. The combination of ND-filters was replaced with a single ND-filter[22], adjusting to the desired intensity.

The changes required repetition of the calibration and parameterization of the optical setup and determination of the gain. The UV-extension created a challenge in the experimental design, as the variations in intensity across the UV-spectrum were significantly larger than those caused by the wavelength selector in the setup for VIS. Ultimately, the gain measurements for the UV spectrum appeared to be systematically shifted. Additionally, the desired intensity range for the detection efficiency measurement, as determined in section 4.1.2, could not be ensured, which likely biased the results as well. Neither the reason for the offset, nor a suiting correction method could be found in the framework of this thesis. Thus, the discussion of the temperature dependence of the DE in the following sections does not include the UV-spectrum. The biases and possible experimental errors in the investigations in the UV-spectrum are discussed in section 4.2.4.

---

[17]FG105LCA by ThorLabs
[18]Model MBT602 by ThorLabs
[19]C-70/350 by CTS
[20]NIM8306 two slot crate with N979B amplifier and NHQ 224M HV-supply by CAEN
[21]NKT Photonics SuperK EXTEND-UV
[22]NDUV04A by Thorlabs

4.2.1 Initial Setup and Parameterization of Optical Components

As the measured current of the reference diodes must be related to the number of photons reaching the PMT photocathode, the optical system linking the two quantities has to be characterized under variation of the wavelength. The idea is to replace the PMT in the setup shown in figure 4.2.1 with a calibrated diode[23] with known quantum efficiency QE_{calib} and measuring the photocurrents I_{calib} at the calibrated PHD and I_{ref} at the reference PHD simultaneously. As the ND-filters inserted in the path guiding to the PMT attenuate the light down to the order of 10^2 photons, undetectable for the PHD, the parameterization of the reference current has to be conducted in two parts. In the first measurement, the photocurrents at the calibrated and reference PHD are measured simultaneously, with the ND-filters removed. Consequently, the transmittance of the used ND-filter combination is determined separately. The calibrated transmittance ratio r_λ can be defined as the ratio of the diode currents without the ND-filters inserted in between, associated to the absolute light flux by the QE of the calibrated PHD QE_{calib}:

$$r_\lambda = \frac{I_{calib}}{QE_{calib} \cdot I_{ref}} \tag{4.2.1}$$

Thus, the total calibrated reference τ_λ for the setup is given by

$$\tau_\lambda = r_\lambda \cdot T_{ND,\lambda}, \tag{4.2.2}$$

with the transmittance of the combination of ND-filters $T_{ND,\lambda}$. Before and after measuring r_λ for all wavelength steps, the ambient light in the enclosures was measured. The difference in ambient light is then linearly interpolated across the timespan of the measurement and was consequently subtracted from the measured photocurrents. To avoid systematic errors due to fluctuations in the ambient light, the measurement was repeated five times and the average was taken subsequently. The average measured calibrated transmittance ratio r_λ is shown in fig. 4.2.2. The negative sign appears because the calibrated PHD measures a positive photocurrent, while the photocurrent measured at the reference PHD is negative. It was found that the combination of two re-

FIGURE 4.2.2: Average calibrated transmittance ratio r_λ over five repetitions. The standard errors are smaller than the markers.

flective ND-filters with optical densities of 2.0 and 3.0 is suited to achieve the desired intensities between 10 - 1000 photons reaching the photocathode per pulse, across the full spectrum. Measuring both ND-filter's combined transmittivities at once is not possible for the intensities provided by the light source, as the transmitted share of light is too dim to be measured with the photodiode. Consequently, the ND-filters transmittivities had to me measured separately. The filters were placed orthogonal to the beam path, with the photodiode behind. For reference, the photocurrent was measured without the filter. Similarly to the measurement of r_λ, before and after measuring the photocurrent for all wavelength steps, the ambient light in the enclosure was measured and then linearly interpolated.
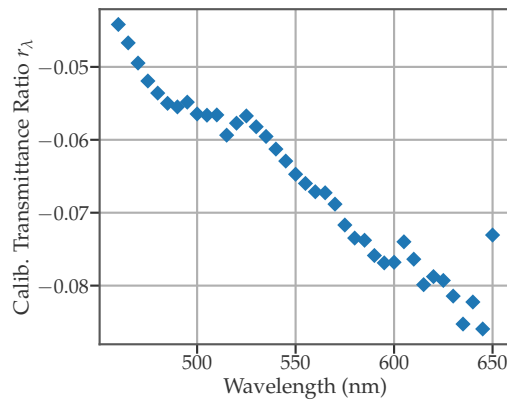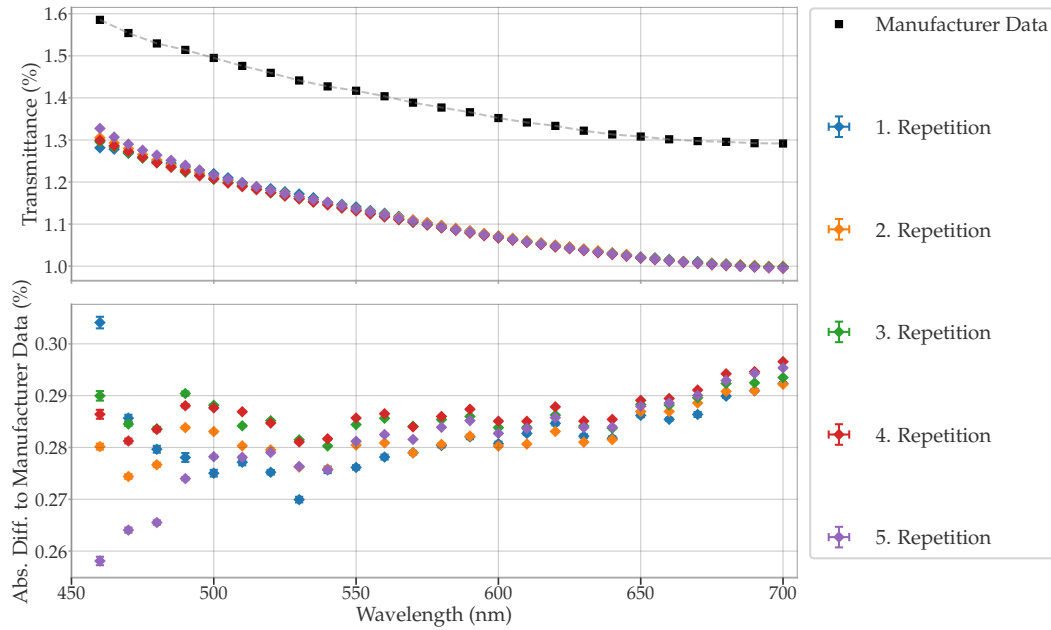
---

[23]Model 818-UV/DB by Newport

FIGURE 4.2.3: Repetitive transmittance measurements to quantify potential angular displacement of the ND-filter with an optical density of 2.0 due to mounting and dismounting. Compared to provided data by the manufacturer [22]. The lower plot shows the absolute difference of the repeated measurement to the data from Thorlabs. The dashed line is purely for visualization purposes.

The measurement was performed five times for the reflective ND-filter with the optical density of 2.0 to check whether the manual placement of the filter in the mount changes the filter's position, potentially increasing or decreasing its transmittance due to a slight change in incident angle. The results for the latter are shown in fig. 4.2.3. As shown in the lower plot, the impact of remounting the filter on transmittance tends to be greater towards shorter wavelengths, causing a higher

TABLE 4.2.1: Mean values of the absolute difference of the measured transmittance to the provided data by the manufacturer [22].

Rep.	Mean abs. difference (%)
1	0.2824(69)
2	0.2822(47)
3	0.2864(34)
4	0.2870(39)
5	0.2813(89)

deviation of the transmittance across the repetitions, which could be the consequence of rising light intensity. However, by repetitively remounting the filter, no monotonous de- or increase of the deviation was observed which is pointed out in the mean absolute difference across the repetitions, shown in table 4.2.1. Thus, mounting and dismounting the filters several times should not cause a systematic change in the effective transmittance of the ND-filters. This is crucial, since cleaning or a change of the filters is potentially necessary throughout the experiments.

For the following measurement of the transmittance of the second ND-filter (OD = 3.0), a single repetition was performed. The measurement data compared to the manufacturer data for both filters is shown in fig. 4.2.4. As already observed for the OD = 2.0 ND filter, there appears to be a constant offset to the data provided by the manufacturer [22] for the OD = 3.0 ND filter as well. Slight variations in performance data are to be expected from filter to filter, according to the manufacturer [22]. Furthermore, the manufacturer's measurement techniques are likely to vary minimally.
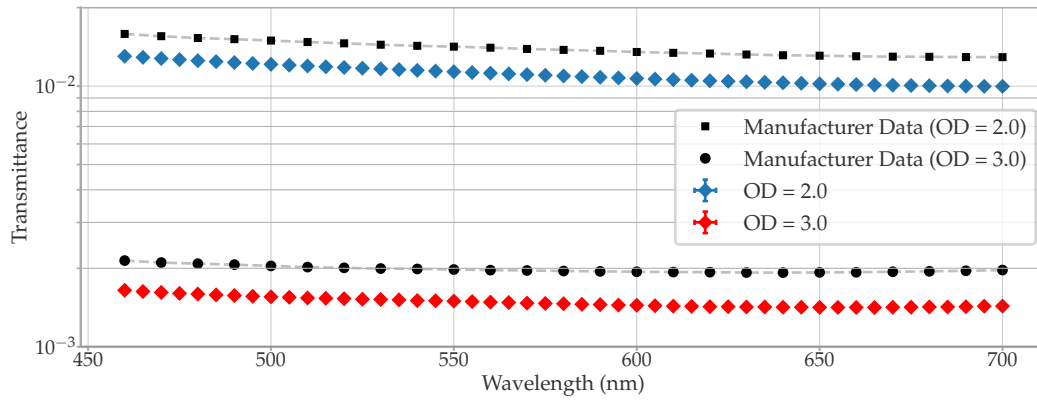
FIGURE 4.2.4: Transmittivities of the used reflective ND-filters with optical densities of 3.0 and 2.0 compared to the corresponding transmittivities provided by the manufacturer [22]. The dashed lines are purely for visualization purposes. The uncertainties are smaller than the markers.

The separate measurement of both ND-filters follows the assumption that the measured transmittivities of both filters can be multiplied for the combination subsequently, obtaining the total transmittance

$$T_{\text{ND},\lambda} = T_{\text{OD2},\lambda} \cdot T_{\text{OD3},\lambda},$$

which ultimately led to the introduction of systematic errors due to inner reflections between the filters, for more detail see appendix A.2.

4.2.2 Determination of the Gain

Based on the gain calibration with the pre-stage setup, the voltage for the PMT was set to $1132\,\text{V}$ for the investigation of the temperature and wavelength dependence of the DE. As the gain is dependent both on the wavelength and temperature itself, it was necessary to conduct a grid scan across the wavelength-temperature space which shall be covered for the detection efficiency measurement. For each wavelength-temperature pair, the charge spectrum of the PMT was fitted, with the charge spectrum model introduced in section 3.4. From each fit, the mean value of the charge distribution corresponding to one single photoelectron Q_1 is obtained. Thus, the gain is simply given by $G = Q_1/e$ for each pair. The measured gain across the wavelength-temperature space is presented in fig. 4.2.5.

In total 468 charge spectra were fitted, to cover the wavelength-temperature space. For the sake of overview, in the left plot of fig. 4.2.5, the determined gains from the fits are not displayed individually, but are represented by trend lines for each temperature step. The shown uncertainty regions are based on the fitting-uncertainty of Q_1, as the square-root of the variance of the fit parameter, which is extracted from the main diagonal of the covariance matrix. As could be suspected from the left side of fig. 4.2.5, cooling could be an uncorrelated effect, which just shifts the spectral gain characteristic to higher gains. On the right side, the difference between the gain and the mean of all measured values across the spectrum for each temperature is depicted. As can be seen, apart from some outliers, the gain increases with the wavelength until it peaks in the region around $\sim 600\,\text{nm}$ for the shown example, after which it decreases again. The wavelength dependence of the gain of the mDOM PMT was previously investigated in [10, p. 58-60], showing comparable results. As this behavior is observable for all observed temperatures (the right side shows only $-40\,^{\circ}\text{C}$ and room temperature for the sake of overview), it is reasonable to suggest that cooling of the PMT in the range of room temperature down to $-40\,^{\circ}\text{C}$ does not influence the spectral characteristic of
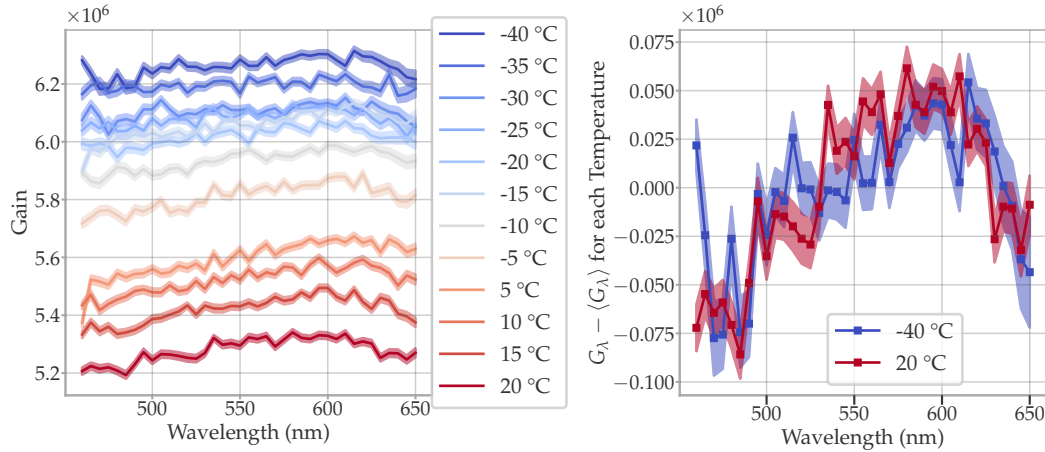
FIGURE 4.2.5: **Left:** Determined gains obtained by fitting the charge spectrum for each wavelength-temperature pair. **Right:** Difference between the gain and the mean of all measured values across the spectrum, exemplary for $-40\,°$C and room temperature. *For both:* The connecting lines are intended to indicate the course of the gain, but have no physical meaning. The uncertainties are represented by the colored regions around the lines.

the gain but generally increases the mean gain over the spectrum observed by $\sim 0.3\,\%\,°\text{C}^{-1}$ relative to the mean gain at room temperature for the spectrum. The continuous increase in gain by cooling was also observed for the mDOM PMT in [10, p. 55-56]. Furthermore, the observed temperature dependence is similar to those found in [23, p. 255-311], in which the temperature dependence of the gain between $-60\,°$C - $20\,°$C was measured. They found an increase in gain by cooling with $\sim 0.2\,\%\,°\text{C}^{-1}$ for a PMT with 12 dynode stages. As suggested in [24], the gain could increase with cooling due to a higher secondary emission yield of the dynode stages. However, [23] pointed out that the increase in measured gain might also stem from a decrease in the resistivity of the signal cable or the base, which would lead to a higher charge measured at the anode.

4.2.3 Detection Efficiency Measurements

The detection efficiency for each temperature-wavelength step is calculated based on the reference photodiode current and the average charge of the PMT response for a given light pulse. For the measurement of the incident flux of the reference photodiode (PHD), the photodiode continuously measures the current. Each current logged by the picoammeter is calculated as the mean value of 20 sub-measurements and is then marked with a timestamp. Simultaneously, the oscilloscope measures 200000 waveforms in batches of 25000 waveforms per temperature-wavelength-pair on the PMT side. Each batch is marked with a timestamp, respectively, so that the logged PHD currents can be matched to the measurement periods. For each temperature-wavelength-pair, the average of the corresponding PHD current is selected as the photocurrent for the measurement period. Generally, it is advisable to measure as many waveforms as possible for each temperature-wavelength pair, as it decreases the uncertainty of taking the average. As the complete measurement covers 468 pairs, the number of waveforms per pair is a crucial time factor. For 200000 waveforms per pair, the standard deviation of the average charge is in the order of $\mathcal{O}(\text{fC})$ while the average charge itself is in the order of $\mathcal{O}(\text{pC})$, which is sufficient for the measurements. To minimize the distortion of the PMT responses by correlated background, like afterpulsing ($\sim 1\,\mu$s - $10\,\mu$s), the repetition rate R

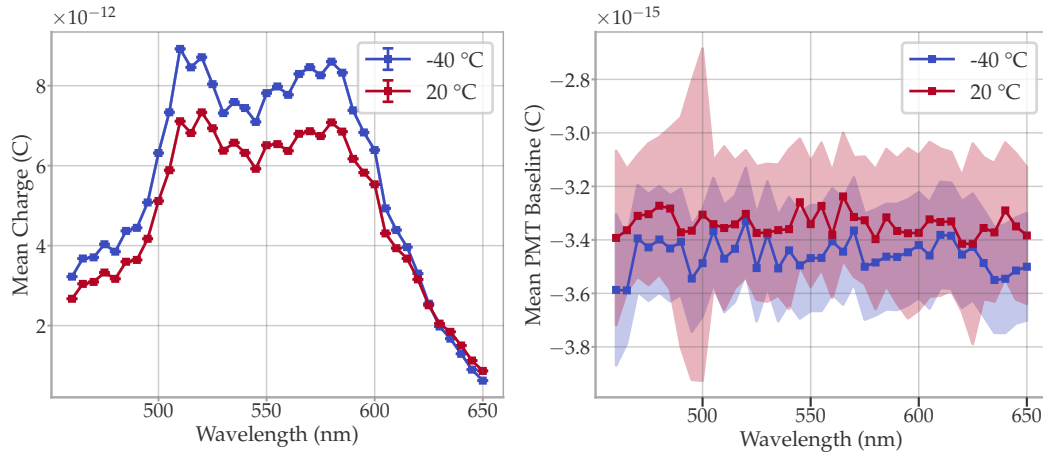FIGURE 4.2.6: **Left:** Mean pulse charge over the spectrum from $460\,\text{nm}$ - $650\,\text{nm}$ for a room temperature and $-40\,^\circ\text{C}$. **Right:** Mean baseline charge for the same wavelength-temperature pairs as on the left. The colored regions represent the uncertainty of the data points. *For Both:* The connecting lines are for purely for visualization purposes, and do not represent measurement data. The uncertainties are smaller than the markers. The other temperature steps are not displayed for the sake of overview.

of the laser was set to $20\,\text{kHz}$, which delivers sufficient light intensity for the reference measurement at the photodiode.

Based on eq. (4.1.1) and eq. (4.2.2), the average number of photons reaching the photocathode per light pulse N_λ is given by

$$N_\lambda = \frac{\tau_\lambda \cdot I_\text{ref}}{R \cdot e} \quad \text{with} \quad \tau_\lambda = r_\lambda \cdot T_{\text{ND},\lambda}, \tag{4.2.3}$$

where τ_λ is the total transmittance ratio of the beam path guiding to the reference photodiode and the beam path guiding to the PMT. It was determined in preparatory measurements, presented in section 4.2.1 and is given by the product of the transmittance of the used ND-filter combination $T_{\text{ND},\lambda}$ and the calibrated ratio of the transmittivities of the beam paths without the filters in between r_λ. As also pointed out in section 4.1.2, the light intensity at the photocathode should not exceed the intensities above or below 10 - $1000\,N_\lambda$, which was ensured by the choice of the ND-filters. Using eq. (4.2.3), the measured variation in N_λ across the temperature-wavelength space of interest could be confirmed to lie between $15.934(94)$ and $275.14(19)$ with an average of ~ 116 photons reaching the photocathode. The average number of detected photons n_λ is calculated with the mean charge method from eq. (4.1.2), with the only difference being that the gain now becomes a temperature and wavelength dependent parameter $G_{T,\lambda}$. Furthermore, the observed systematic error concerning the subtraction of the mean charge of the baseline $\langle Q_{bkc} \rangle$ presented in section 4.1.2 is now tackled by avoiding a shift of the baseline in the order of $\mathcal{O}(\text{pC})$ by adjustment of oscilloscope settings. The resulting mean charges and baselines are shown in fig. 4.2.6. As the mean charge is mainly in the order of $\mathcal{O}(\text{pC})$ and the baseline shift is near zero in the order of $\mathcal{O}(\text{fC})$, which is in the same order as the uncertainty of the mean charges displayed on the left, the subtraction of the baseline can be considered negligible. Ultimately, inserting eq. (4.2.3) and eq. (3.2.2) in eq. (3.2.1), the absolute detection efficiency was determined for each selected temperature-wavelength pair as

$$\text{DE}(\lambda, T) = \frac{\langle Q_\text{PMT} \rangle (\lambda, T) \cdot R}{G(\lambda, T) \cdot \tau_\lambda \cdot I_\text{ref}(\lambda, T)}. \tag{4.2.4}$$

The resulting DE for room temperature and $-40\,°C$ are exemplarily shown in fig. 4.2.7 for the observed wavelength steps. Similar characteristics were observed in [10, p. 71] for the exact same PMT (Serial. Nr. BA0784). What is striking about the DE in fig. 4.2.7, when compared to the spectral DE determined in [10, p. 71], are the *kinks* appearing at lower wavelengths, seemingly independent of the temperature. This systematic error was caused by optical phenomena appearing, when placing the reflective ND-filters behind each other, for an extensive discussion see appendix A.2. However, the effect does only distort the absolute values of the detection efficiency, but not the relative values of the DE to the DE at room temperature (DE_{RT}), or the temperature dependence of the DE significantly, since it only slightly distorts $T_{ND,\lambda}$, which is independent of temperature. This can be seen in fig. 4.2.8, which shows the detection ef-

FIGURE 4.2.7: Absolute detection efficiency for room temperature and $-40\,°C$ across the visible spectrum. The connecting lines are for purely for visualization purposes, and do not represent measurement data. The uncertainties are smaller than the markers.

ficiency relative to that at room temperature. If $DE/DE_{RT} > 1$, the detection efficiency thus increases by cooling to the corresponding temperature, whereas for $DE/DE_{RT} < 1$ the detection efficiency decreases by cooling. The systematic distortions, which appeared for the blue end of the spectrum, are not relevant, if relative values of the detection efficiency are investigated. The figure shows that whether the DE increases or decreases by cooling is highly dependent on the wavelength. In general, fig. 4.2.8 suggests that cooling amplifies
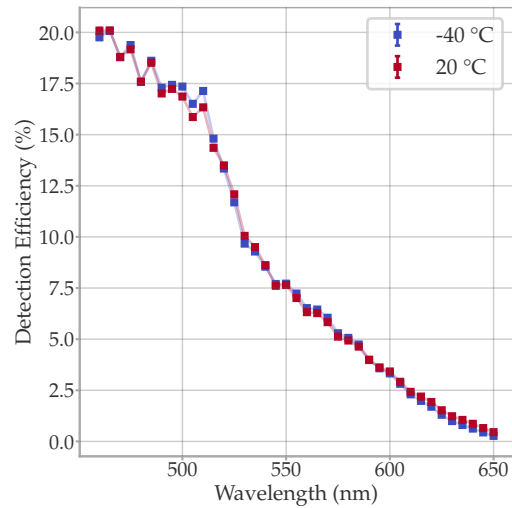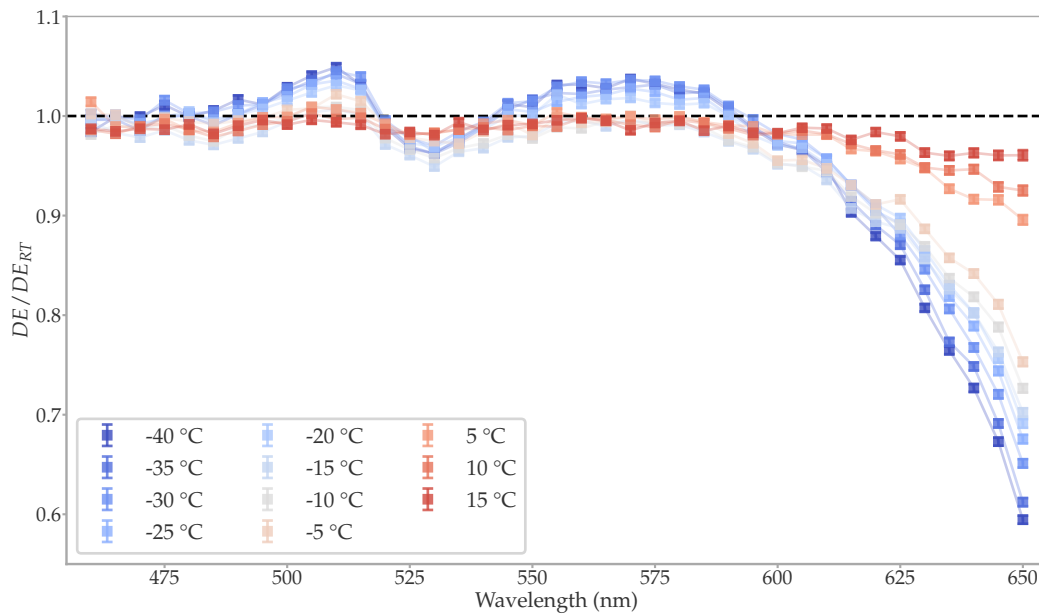

FIGURE 4.2.8: DE for all temperatures observed, relative to the DE at room temperature. The connecting lines are for purely for visualization purposes and do not represent measurement data. The uncertainties are smaller than the markers.
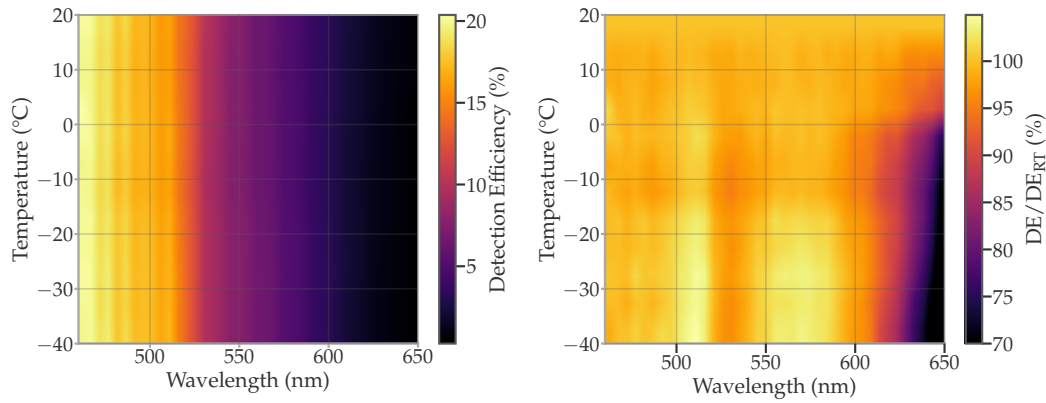
FIGURE 4.2.9: Absolute detection efficiency (left) and relative detection efficiency to room temperature (right) across the investigated parameter space. Bilinear interpolation was used to smooth the heatmap.

the extrema of the characteristic peaks of DE/DE$_{RT}$ but does not affect the position of the extrema. The complete investigated parameter space of both, absolute DE and DE/DE$_{RT}$ are shown in fig. 4.2.9. Considering the absolute detection efficiency (left), again it is apparent, that the systematic error produces temperature independent *kinks*, which are most noticeable at shorter wavelengths, while the relative detection efficiency features no comparable systematic distortions.

It is necessary to process the obtained data, to quantify how cooling in the range from room temperature down to $-40\,°C$ affects the detection efficiency per $°C$. Therefore, the detection efficiency relative to that at room temperature as function of temperature is fitted linearly, as introduced in eq. (3.2.3), to obtain the temperature dependence coefficient $\alpha_{DE}(\lambda)$. The applied linear fits[24] are shown in fig. 4.2.10 for a selection of representative wavelengths. The reader shall be reminded that the linear approximation of the temperature dependence of
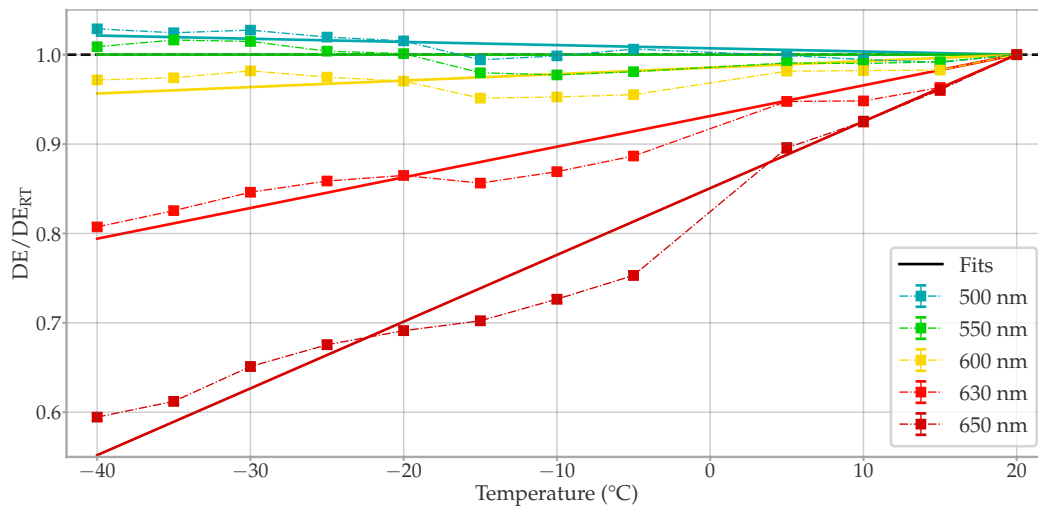

FIGURE 4.2.10: Linear fitting of the detection efficiency relative to that at room temperature, as introduced in eq. (3.2.3). The coloring of the data corresponds to the visible spectrum. The connecting dash-dotted lines are for purely for visualization purposes, and do not represent measurement data. The uncertainties are smaller than the markers.

---

[24]Fit Method: Orthogonal Distance Regression (`scipy.odr`)

the DE does not describe the real nature of the de- or increase of the DE with temperature, as the slope varies over the observed temperature range systematically, for the observed spectrum. Nevertheless, the relative deviations of the real characteristic to the fitted slope is under $\pm 8\,\%$ across the temperature-wavelength space investigated. The validity of defining a linear temperature dependence coefficient must be treated carefully. For this thesis, considering the deviations from linear behavior, it was deemed appropriate to define $\alpha_{\mathrm{DE}}(\lambda)$. To the author's understanding, there exists no research that explores the temperature dependence of the DE or QE of PMTs with bialkali photocathodes across a comparable temperature range with similar resolution. As for [25], it is not clear, which temperature was used for normalization, nor if the y-intercept of the slope was forced, like in this thesis. This would be relevant, as it could be argued, that leaving the y-intercept as a free fitting parameter, the best linear approximation could be fit to the relative DE's temperature dependence.

The resulting slopes of the linear fits are presented in the upper plot in fig. 4.2.11. The decreasing slopes of the DE relative to that at room temperature, thus negative $\alpha_{\mathrm{DE}}(\lambda)$ represent the wavelengths at which cooling the PMT down from room temperature increases the DE, while positive $\alpha_{\mathrm{DE}}(\lambda)$ correspond to the wavelengths at which cooling decreases the DE. The most striking feature of the temperature characteristic, shown in fig. 4.2.11, is the high rise of $\alpha_{\mathrm{DE}}(\lambda)$ approaching the cut-off wavelength λ_0, at which $\alpha_{\mathrm{DE}}(\lambda)$ reaches over $0.7\,\%\,°\mathrm{C}^{-1}$ of DE at room temperature at the red end of the observed spectrum at $650\,\mathrm{nm}$. It could be suspected that this high relative increase DE by temperature in the red end of the investigated
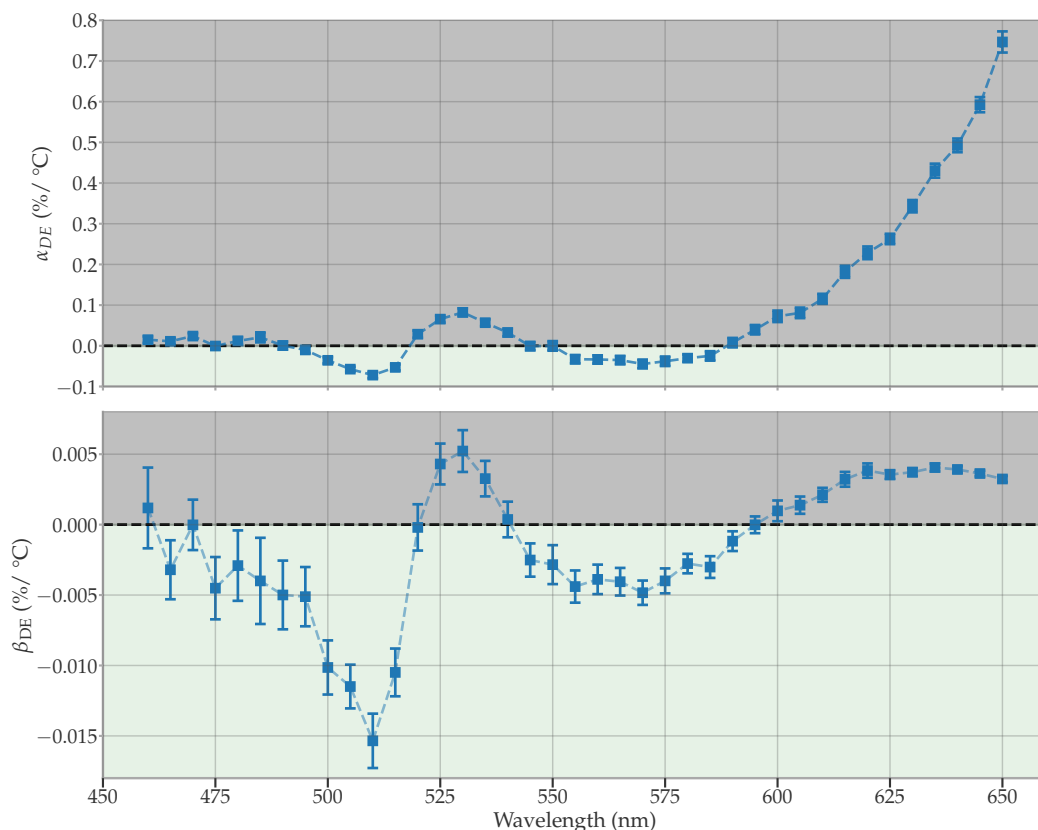

FIGURE 4.2.11: Temperature coefficients $\alpha_{\mathrm{DE}}(\lambda)$ and $\beta_{\mathrm{DE}}(\lambda)$ for the observed region of the visible spectrum. Note that $\alpha_{\mathrm{DE}}(\lambda)$ is in % of the relative detection efficiency to room temperature, while $\beta_{\mathrm{DE}}(\lambda)$ is in % of the absolute detection efficiency. The connecting dash-dotted lines are for purely for visualization purposes, and do not have physical meaning. The uncertainties are often smaller than the markers.

spectrum might not directly be correlated to the wavelength, but more to the low absolute detection efficiency in this region, approaching $0\,\%$, see fig. 4.2.7. If the photocurrents at the photocathode approach zero, the share of the background current increases significantly. In connection, the background current contributes to photoelectrons emitted without external light, which is referred to as dark rate. A relative increase of the dark rate would imply that effects, such as thermionic emission, could contribute a significant part to the emitted photons by the photocathode. The temperature dependence of the dark rate for the mDOM PMT was investigated extensively in [10, p. 105-127]. It was found, that approaching room temperature, the dark rate significantly increases, [10, p. 108], where thermionic background dominates the background [26]. Since the temperature range observed in this work covers room temperature, the high rate of electrons emitted due to thermionic background relative to the low rate of photoelectrons released by the photoeffect might cause the sharp increase of α_{DE}. Looking back at fig. 4.2.9, this could explain, that while for temperatures below about $0\,^{\circ}\mathrm{C}$ the relative DE does decrease drastically to down to below $70\,\%$ for wavelengths above $\sim 600\,\mathrm{nm}$. where the absolute DE is vanishing, while sustaining over $90\,\%$ for higher temperatures.

The temperature-dependence of the photocurrent was investigated in the UV spectrum across a larger temperature scale of partially down to $-175\,^{\circ}\mathrm{C}$ - $25\,^{\circ}\mathrm{C}$ in [17]. Among one other PMT, the Hamamatsu R1668 was studied, which features a $\varnothing 25\,\mathrm{mm}$ bialkali photocathode. They observed that the relative photocurrent suddenly decreases for temperatures below about $-125\,^{\circ}\mathrm{C}$, ultimately vanishing at around $-125\,^{\circ}\mathrm{C}$, after not changing more than a few percents from room temperature down to $-50\,\%$. In [17], the decrease was associated with the temperature dependence of the normalized resistivity (relative to $0\,^{\circ}\mathrm{C}$), which was approximated by $e^{-\beta T}$, where β is a material-specific constant. It was noted, that due to the semiconductor nature of the photocathode, the results vary from this approximation, however the increase of resistivity described to vanish in relative photocurrent. As the temperatures investigated in this thesis are in the region of above $-40\,^{\circ}\mathrm{C}$, the change in resistivity of the photocathode might not be the dominant factor for the determined α_{DE}, but is more likely to be governed by interdependencies in the semiconductor nature of the photocathode.

For lower wavelengths, two regions can be identified, in which cooling enhances DE, reaching $\sim 495\,\mathrm{nm}$ - $515\,\mathrm{nm}$ and $\sim 545\,\mathrm{nm}$ - $585\,\mathrm{nm}$, respectively. In these regions, DE increases up to $0.0720(75)\,\%\,^{\circ}\mathrm{C}^{-1}$ relative to room temperature, when the PMT is cooled down, peaking at $\sim 510\,\mathrm{nm}$ and $\sim 570\,\mathrm{nm}$ for the two valleys, respectively. The valleys are separated by a region between $\sim 520\,\mathrm{nm}$ - $540\,\mathrm{nm}$, for which the DE decreases slightly to up to $0.0823(97)\,\%\,^{\circ}\mathrm{C}^{-1}$ when the PMT is cooled down. Similar characteristic were observed in [25] for the same photocathode material. Since it is unclear, which temperature was used for normalization in [25] and that the temperature range slightly differs ($-20\,^{\circ}\mathrm{C}$ - $40\,^{\circ}\mathrm{C}$), the comparison of the studies should be treated with caution. It is to be noted, that even though the cathode material is the same in [25], the ratio of the compounds and photocathode size and shape differs. However, as the cut-off wavelength λ_0 of the mDOM PMT is about $700\,\mathrm{nm}$ [27], it is interesting to compare the characteristics from [25], which feature the temperature dependence coefficient for bialkali photocathodes with $680\,\mathrm{nm}$ and $700\,\mathrm{nm}$, which is shown in fig. 4.2.12. The characteristic increase in α_{DE} approaching λ_0 equally appears for both PMTs investigated in [25]. It stands to reason that the increase of α_{DE} approaching λ_0 is correlated with the relative increase in background caused by the high background relative to the vanishing number of photoelectrons released due to the photoeffect, which would agree with the shifts in the increases to higher wavelengths for higher λ_0. Comparing the mDOM PMTs temperature characteristic with the PMT of [25] with $\lambda_0 = 720\,\mathrm{nm}$, it stands out, that the local maxima at $\sim 535\,\mathrm{nm}$, which is featured in the characteristic of the
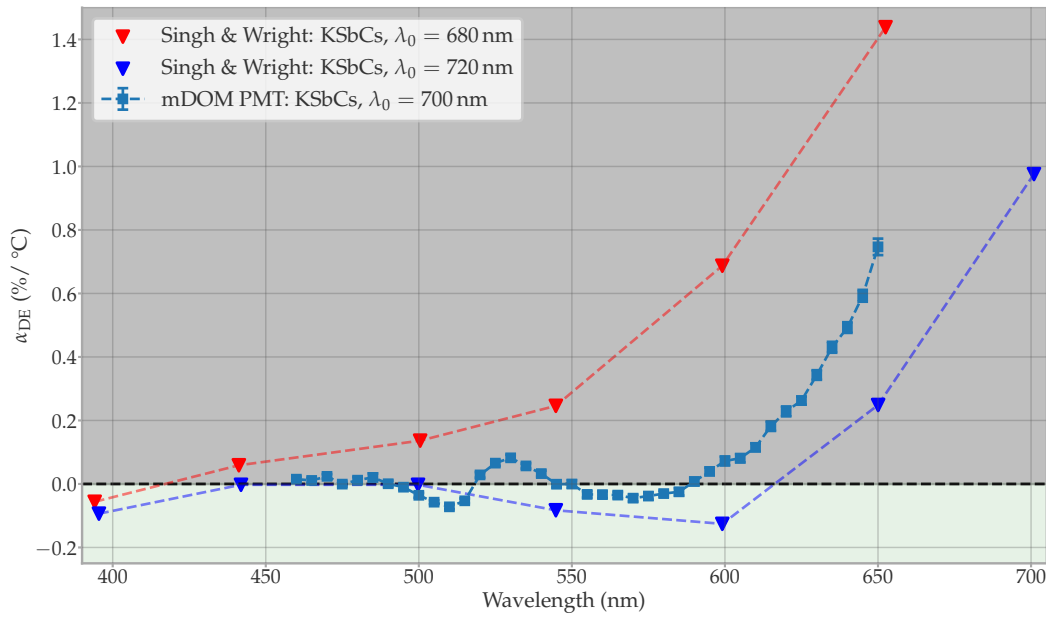
FIGURE 4.2.12: Temperature coefficients $\alpha_{\mathrm{DE}}(\lambda)$ from [25] compared to the determined coefficient in this work for the mDOM PMT (same as shown in fig. 4.2.11). The connecting dash-dotted lines are for purely for visualization purposes, and do not represent measurement data. The uncertainties are often smaller than the markers.

mDOM, is not seen for the PMT with $\lambda_0 = 720\,\mathrm{nm}$. This could be a result of the low spectral resolution chosen in [25]. However, it remains possible that local extrema are the result of the differences in the material properties, likewise. The systematic increase of measured relative detection efficiency measured by temperature near the cut-off wavelength has also been schematically indicated in [26, p. 246] for a number of other photocathode materials. It appears reasonable to propose that the observed increase in DE is skewed by the surge in thermionic emission at elevated temperatures, resulting in the detection of electrons not emitted through the photoelectric effect.

The temperature coefficient $\beta_{\mathrm{DE}}(\lambda)$, describing the temperature dependence of the absolute DE, is also determined, as introduced in eq. (3.2.4). In contrast to $\alpha_{\mathrm{DE}}(\lambda)$, which highlights for which wavelengths the detection efficiency is most sensitive to changes in temperature, $\beta_{\mathrm{DE}}(\lambda)$ points out how significant the in- or decrease the detection efficiency is as a consequence of a change in temperature in absolute terms. The reader should be reminded that α_{DE} is expressed in terms of % relative to $\mathrm{DE}/\mathrm{DE}_{\mathrm{RT}}$ per °C, whereas β_{DE} is measured in % of the absolute DE per °C. For a linear temperature dependence, the difference of the coefficients is purely in the normalization. Hence, the signs of the coefficients should not differentiate for each wavelength across the spectrum and should only differ by scaling factor. However, as a look at the bottom plot of fig. 4.2.11 reveals, the sign of the coefficients does differentiate for some wavelengths. This contradiction appears due to the normalization used, which skews the parameter space, potentially affecting the fitted slope. For $|\beta_{\mathrm{DE}}| \to 0$ this can result in change of the sign, as most perceptible for lower wavelengths below $\sim 500\,\mathrm{nm}$ in this case. It is also to mention, that β_{DE} is biased by the systematic error discussed in appendix A.2, as it one-sidedly decreases the measured DE compared to the unbiased DE, while the normalization by $\mathrm{DE}_{\mathrm{RT}}$ eliminates the bias for α_{DE}. Putting the systematic distortions aside, a major difference in the characteristics of the coefficients is the trend of $\beta_{\mathrm{DE}}(\lambda)$ for wavelengths approaching λ_0. Since the absolute DE vanishes approaching λ_0, even though the DE increasingly sensitive to changes in DE resulting in a high $\alpha_{\mathrm{DE}}(\lambda)$, the increase of $\beta_{\mathrm{DE}}(\lambda)$

stagnates at $\sim 625\,\mathrm{nm}$ approaching λ_0. The operating temperatures for the mDOM are expected to lie between $-20\,^\circ\mathrm{C}$ and $-30\,^\circ\mathrm{C}$ as a function of depth, as introduced in section 2.3. For the highest observed absolute value of $\beta_{\mathrm{DE}}(\lambda)$ at $510\,\mathrm{nm}$, this would imply a maximum difference of $\sim 0.15\,\%$ DE from the highest to the deepest deployed mDOM. However, as outlined in section 2.2, the typical wavelengths of the Cherenkov radiation are in the UV-range or in the blue end of the visible spectrum. For the latter, the determined β_{DE} between 460 - 520 indicate a positive effect of cooling on the DE.

It remains questionable whether the temperature-difference-induced increases in detection efficiency of under approximately $\sim 0.15\,\%$ across the depths of IceCube Upgrades mDOMs for the blue end of the visible spectrum are relevant for event reconstruction. [10, p. 71] found that the absolute DE also varies from PMT to PMT in the order of several percents. If the DE of all PMTs for IceCube Upgrade is not measured in isolation beforehand, taking the average is necessary, which might introduce an uncertainty in the order of %. Thus, the temperature-difference-induced shifts in DE might not be relevant. To evaluate the significance for IceCube Upgrade, extensive studies on a higher number of mDOM PMTs are necessary. Nevertheless, this is only said for the blue end of the visible spectrum. To cover the full spectrum of interest for IceCube, an investigation of the temperature dependence in the UV-range is necessary. However, in the framework of this thesis, the experimental conditions for the measurement of the gain and the DE could not be realized in the available time. The challenges and corresponding solution approaches concerning the investigation of the DE in the UV-spectrum are presented in section 4.2.4.

The temperature dependence of DE is anticipated to be largely influenced by the photocathode material's temperature dependence, reflecting in the QE contribution. The collection efficiency F, however, is purely dependent on the electric field between the photocathode and multiplication system and the field between the dynodes, determining the position on the dynodes where the photoelectrons and primary electrons are directed to, respectively. As F is defined as the likelihood of the photoelectron or primary electron to *reach* the next dynode, As long as secondary electrons are emitted at each dynode stage, a reduction in the stage gains due to temperature affects only the total gain. Thus, the measured F should remain largely unaffected by temperatures within the observed range from room temperature to $-40\,^\circ\mathrm{C}$.

To the best of the author's knowledge, previous studies on the detection efficiencies of PMTs are mainly of empirical nature, focussing on use-cases of the specific PMT-type. However, there are analytical models to describe the quantum efficiency of semiconductor photocathodes, as Spicer's three-step model [28], which is widely used and modified to describe photoemission processes in semiconductors. The main assumption for semiconductors is that the released photoelectron predominately scatters with the lattice. The temperature dependence then is modelled with Bose-Einstein statistics, which the phonon population of the material underlies. It is to be expected that modelling the quantum efficiency of a specific PMT type as the R15458-02 by Hamamatsu is a major challenge, as it requires detailed knowledge of the photocathodes material properties. Moreover, to obtain the detection efficiency, the collection efficiency must be investigated, as recently conducted via computer simulations in [29], which will be continued in [30] soon.

4.2.4 Investigations in the UV-Spectrum: Evaluation of Methodological Bias and Errors

In order to investigate the temperature dependence of the DE in the UV-spectrum, the setup for the visible spectrum had to be adapted, in the form of the replacement of the wavelength selector with an UV-extension. Consequently, the optical setup and parametrization described section 4.2.1 as well as the gain measurement (section 4.2.2) were repeated for the UV-spectrum.

During the determination of the gain for the UV spectrum, a significant shift occurred in contradiction to the gain determined in the blue end of the visible spectrum (VIS), as shown in fig. 4.2.13. As seen in the overlap region of both spectra, the determined gains are consistently offset across all temperature steps. Comparable contradictory gain shifts were observed when replacing the wavelength selector with the UV-Extension in a previous work [31, p.32-33]. In this work, no explanation attempt was proposed. In [10, p. 58] it was proposed that the offset could partially be related to non-Poissonian photon counting statistics of the laser system, which are not considered in the fitting model used, based on eq. (3.4.2). In the latter work, a modified fitting model was used alternatively, which does not weight the Gaussian charge contributions with the probability from the Poisson distribution inherently, but leaves it as a free parameter.

However, the light intensities during the gain measurements in this thesis were too high to adapt this method, as for increasing numbers of Gaussian distributions significantly contributing to the convolution, the free fitting of their amplitudes gets successively more difficult. As can be seen in the figure fig. 4.2.14, the mean number of photoelectrons reaching the multiplication system μ is in the order of $\sim 1-5\,\mathrm{PE}$ for wavelengths above around $395\,\mathrm{nm}$. In [10, p. 59] the number of Gaussians n was truncated to $n = 3$ to avoid introducing too many free variables. As for higher μ, contributions of $n > 3$ are significant, the truncation cannot be used in this work. Allowing higher contributions inevitably comes with the introduction
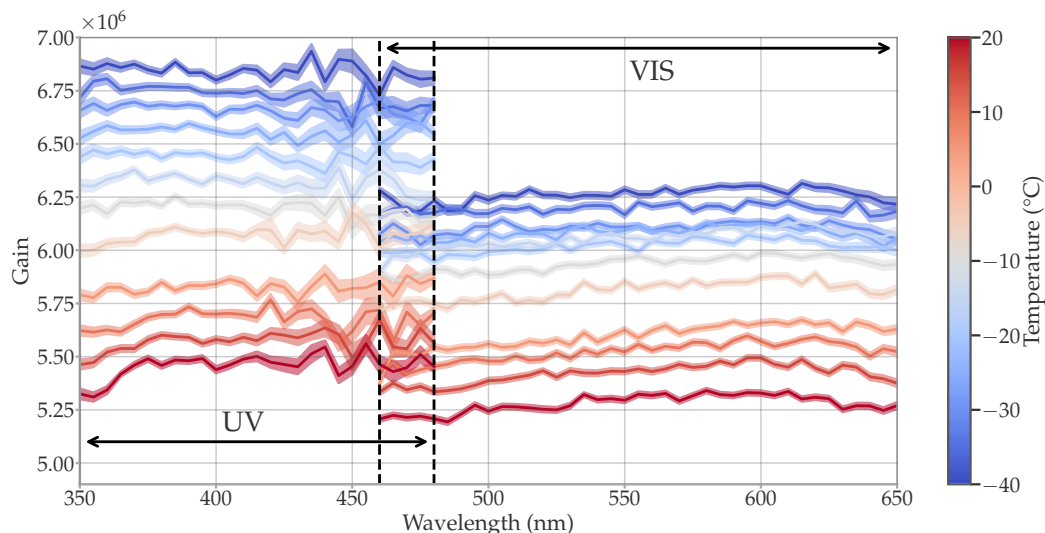

FIGURE 4.2.13: Determined gains obtained by fitting the charge spectrum for each wavelength-temperature pair. The UV-spectrum and visible spectrum (VIS) had to be measured with changing setups, resulting in a systematic shift in the determined gains. The connecting lines for the spectral gains at each temperature are drawn instead of the total of 792 data points for the sake of overview. The uncertainties are represented by the colored regions around the lines.
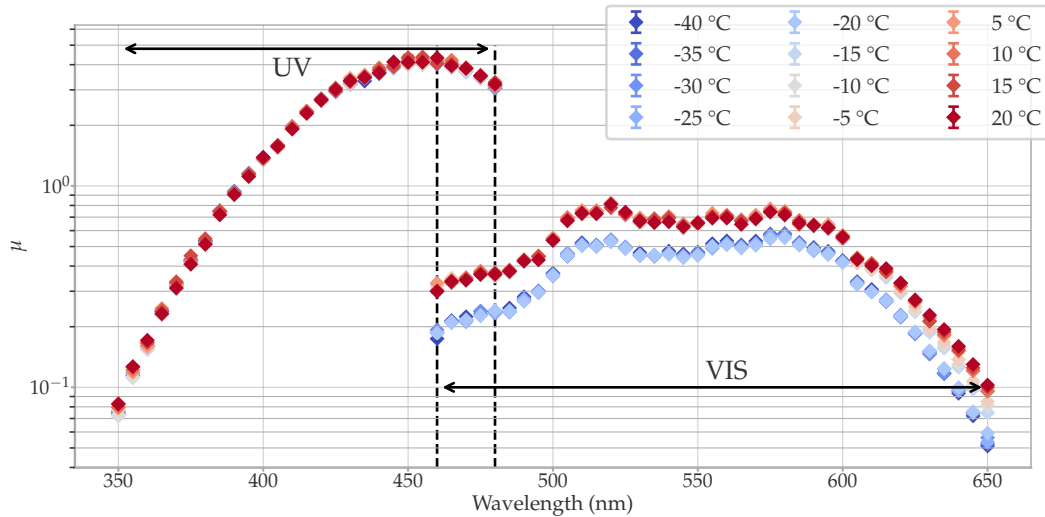
FIGURE 4.2.14: Mean number of photoelectrons reaching the multiplication system μ obtained by charge fits for the UV- and VIS spectrum. The uncertainties are often smaller than the markers.

of more free variables, which ultimately prevented the use of this method in this thesis. To ensure that the intensities are not too high for the modified fitting method, the attenuation of the laser could be decreased by one order via selection of ND-filters for $\lambda > 395\,\text{nm}$. Unfortunately, the setup was already disassembled at the point of realization, preventing to test the modified fitting method.

It should be also considered that for higher μ, the pedestal is often subdominant, which can decrease the goodness of the fit, see appendix A.1. While for the visible spectrum it could be ensured that $0.1 \lesssim \mu \lesssim 1$ via selection of ND-filters, as μ only deviated to the extent of one order, the variation of μ produced by the UV-extension reaches across two orders of μ for the spectrum between $350\,\text{nm}$ - $480\,\text{nm}$. The higher span of intensities in the UV setup compared to those of the VIS setup is the result of the use of the UV-Extension. Suboptimal intensities could be prevented by adjusting the intensity at least once across the UV spectrum to achieve $0.1 \lesssim \mu \lesssim 1$.
The intensity could be controlled by adjusting the attenuation of light with the targeted selection of ND filters. However, the reader should be reminded that attenuation purely shifts the intensity range to higher or lower orders, which is why a change of filters would be necessary for across the UV-spectrum. Again, this could not be applied as the setup was already disassembled at the point of realization.

It might be proposed that the established gains for the UV region can be adjusted to correspond to the visible spectrum in the overlap area. Subtracting the mean difference of the VIS gains in the overlap region from the gain in the UV-spectrum for each temperature step seems to stand to reason, as the wavelength dependence is typically subdominant to the temperature dependence. This aligns both gains with each other, but is purely to be treated as a reference for how the systematic gain shift could potentially distort the resulting DE. The resulting alignment is shown in fig. 4.2.15. It is advisable to investigate the effect of the offset further, as the origin of the phenomenon could also not been found in previous studies on this topic [10, 31]. Given the limited time, the measurement method could not be adapted within the context of this thesis to exclude potential origins of the shift, thus the investigation of this effect would be highly relevant for further PMT sensitivity studies in the UV-spectrum.
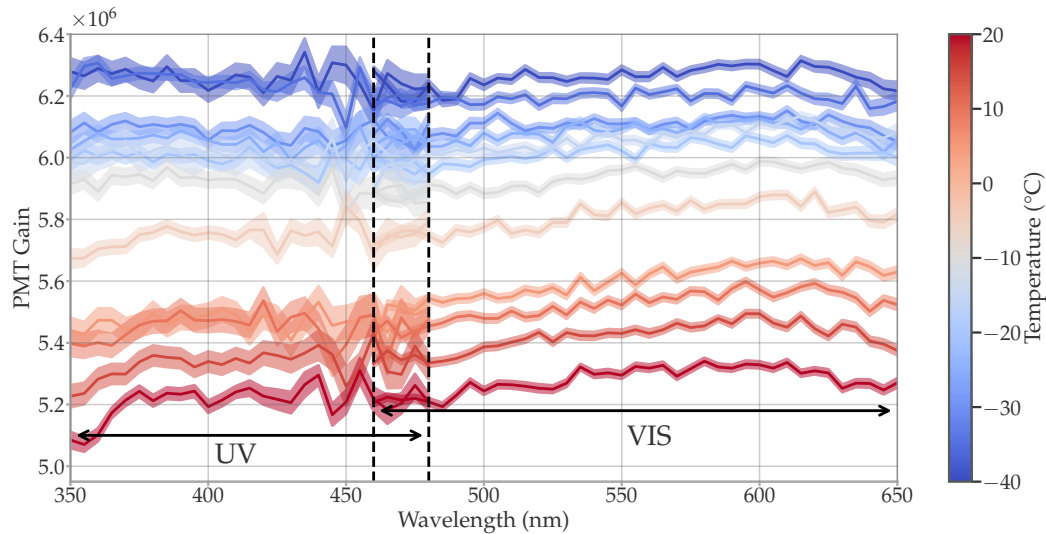
FIGURE 4.2.15: Aligned spectral gains for the UV-spectrum to the visible spectrum (VIS) based on subtraction of the difference in the overlap region. The connecting lines for the spectral gains at each temperature are drawn instead of the total of 792 data points for the sake of overview. The uncertainties are represented by the colored regions around the lines.

Apart from the gain measurement, the increase of variation of light intensity for the UV-range also led to difficulties ensuring that the average number of photons reaching the photocathode N is within the limits of 10 - 1000 photons, approximated in section 4.1.2. As shown in fig. 4.2.16, the intensities for wavelengths under $365\,\text{nm}$ fall below the latter limits. Again, due to time constraints, this could not be corrected by adjusting the light intensity for lower wavelengths.

The bias in the determined gain and potentially also the average number of photons reaching the photocathode N_λ distort the subsequent values of the detection efficiency. As can be seen in fig. 4.2.17, the offset in the gain is reflected in the DE, evident in the overlap region of the spectra observed in both setups. The alignment of the gain decreases the deviation of the DEs from both setups in the overlap regions to between $0.429(59)\,\%$ - $0.656(39)\,\%$ relative to the DE obtained with shifted gain. Still, a significant deviation is noticeable, which is most likely
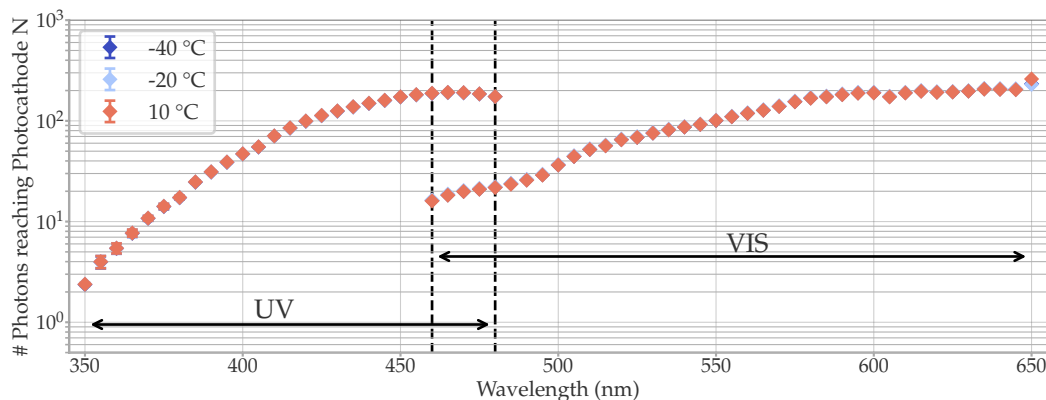

FIGURE 4.2.16: Average number of photons reaching the photocathode for the UV- and VIS spectrum. The uncertainties are mostly smaller than the markers.
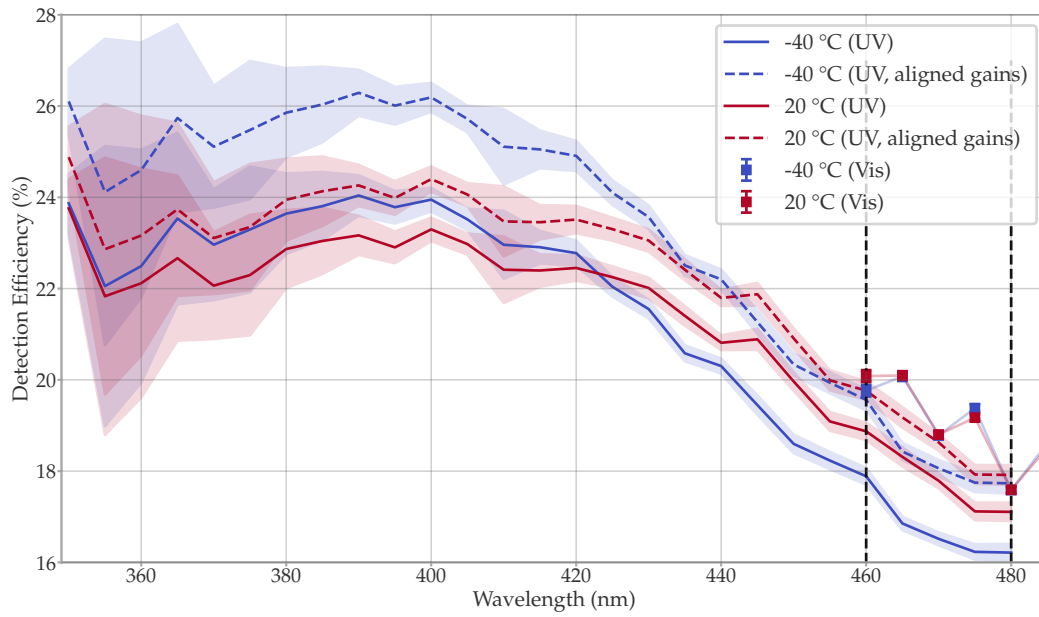
FIGURE 4.2.17: Consequences of the alignment of the gains in the UV spectrum to the visible spectrum, as seen in fig. 4.2.15 on the absolute DE. The uncertainties in the UV-region are depicted as intervals around connecting lines between the determined values for the sake of overview. However, the connection of the values is purely for visualization purposes and has no physical meaning.

the result of the systematic error regarding the ND filters for the VIS setup, as described in appendix A.2.

It is relevant to verify that the gain shift is the dominant systematic distortion, that causes the shift, as N_λ could also be biased. To facilitate this verification, comparing the resulting detection efficiency to $\langle Q \rangle_\lambda / N_\lambda \cdot e = \text{DE} \cdot G_\lambda$, thus, the remaining parameters without the gain, is helpful. As can be seen in fig. 4.2.18 no systematic shift is recognizable in the overlap region for $-40\,°\text{C}$ and room temperature. The other temperatures are not shown for the sake of overview. It should be noted that at $350\,\text{nm}$ the determined DE as well as
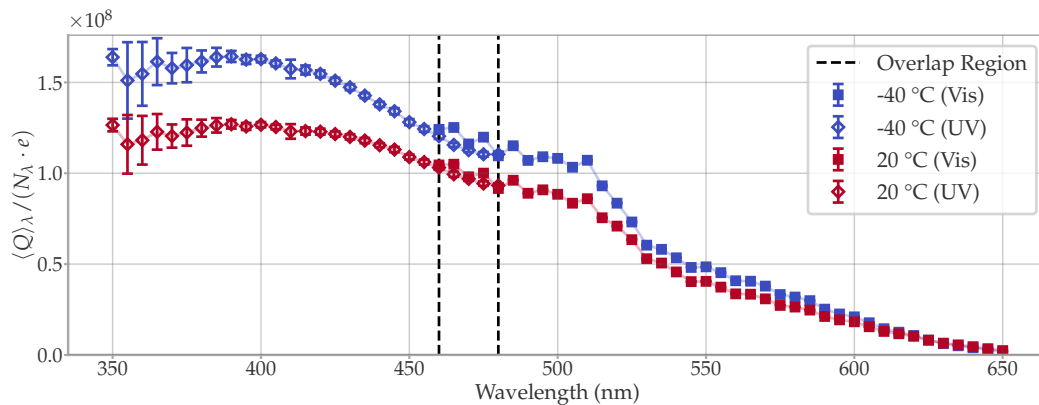

FIGURE 4.2.18: All defining quantities of the DE, apart from the gain across the overlapping spectra covered by the UV and VIS setup $\langle Q \rangle_\lambda / N_\lambda \cdot e = \text{DE} \cdot G_\lambda$ for $-40\,°\text{C}$ and room temperature. The uncertainties can be smaller than the markers. The connecting lines are for visualization and have no physical meaning.

$\langle Q \rangle_\lambda / N_\lambda \cdot e = \mathrm{DE} \cdot G_\lambda$ increases relative to higher wavelengths, which is unexpected, as investigations of the QE for the mDOM PMT indicated a monotonous decrease approaching lower wavelengths under $360\,\mathrm{nm}$ [10]. The upward deviation could be the consequence of the fact that for this wavelength, the average number of photons reaching the photocathode $N_\lambda \approx 2$ falls below the limits suited for the mean charge method as described in section 4.1.2. For $N_\lambda \approx 2$ an upward deviation of about 1% DE is expected, according to the determined deviations shown in fig. 4.1.4, for the mean charge method, meaning obtaining the average number of detected photons n_λ with eq. (3.2.2).

The significant biases in the detection efficiency for each temperature consequently also affect the absolute and relative temperature dependence of the detection efficiency, described by β_{DE} and α_{DE}, respectively. As previously, the magnitude of the offset is apparent for the overlap region, where the results of both setups do not agree, as depicted in fig. 4.2.19. For α_{DE} the alignment of the gain predominantly shifts the temperature dependence constantly upward with a mean difference of $0.063\,41(51)\,\%\,°\mathrm{C}^{-1}$ of relative DE. For β_{DE} similar behavior is evident with a difference of $0.017\,52(50)\,\%\,°\mathrm{C}^{-1}$ of absolute DE. Similarly to the detection efficiency, the alignment of the gain decreases the offset of the characteristics in the overlap region, due to the consequences of the systematic gain shift. However, the reader should be reminded that the alignment does not represent a correction of the gain. The effect of the shifted gains potentially distorts the wavelength dependence of the gain as well, which cannot be accounted for by shifting the gain with a constant factor for all wavelengths. At this stage, it is crucial to locate the origin of the shift before an interpretation of the temperature dependence is attempted.
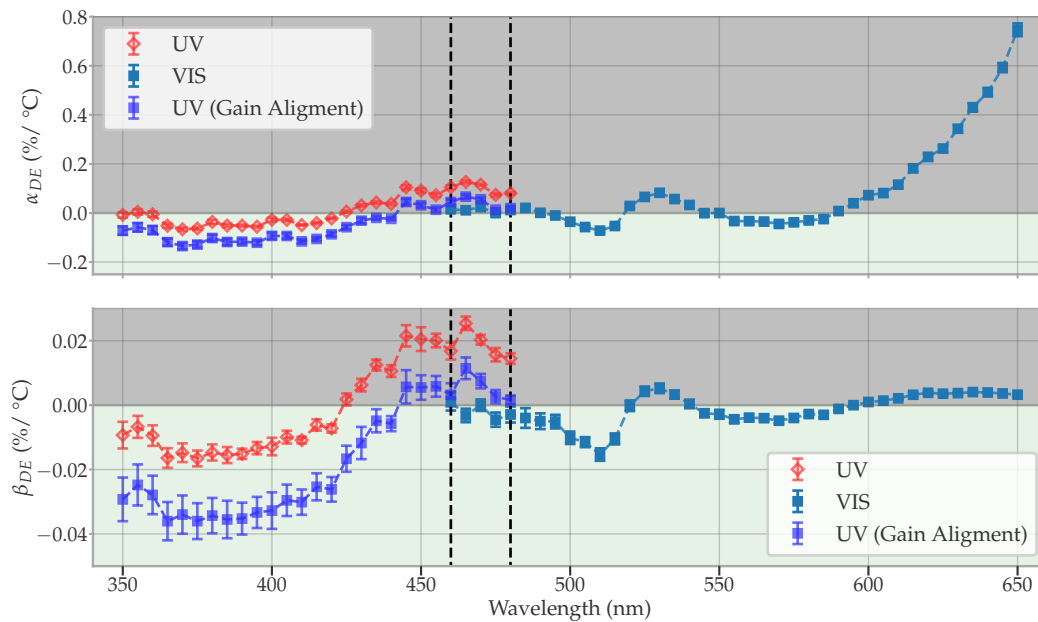

FIGURE 4.2.19: Temperature coefficients $\alpha_{\mathrm{DE}}(\lambda)$ (top) and $\beta_{\mathrm{DE}}(\lambda)$ (bottom) determined based on the UV and the visible spectrum (VIS) setups, compared to the resulting temperature dependence resulting from the gain alignment (see fig. 4.2.15). The reader should be reminded that $\alpha_{\mathrm{DE}}(\lambda)$ is in % of the detection efficiency at room temperature, while $\beta_{\mathrm{DE}}(\lambda)$ is in % of the absolute detection efficiency. The connecting dash-dotted lines are for purely for visualization purposes, and do not have physical meaning. The uncertainties can be smaller than the markers.

5 Summary and Outlook

This thesis aimed to investigate the temperature dependence of the detection efficiency of the mDOM PMT for operating temperatures of between around $-30\,^{\circ}$C and $-20\,^{\circ}$C, which the device will be exposed to, when deployed in the Antarctic Ice with IceCube Upgrade. The detection efficiency, as the total probability of a photon being detected by a PMT, plays a crucial role in the characterization of the overall sensitivity. The detection efficiency is highly sensitive to the wavelength of the incident light, which is mainly the result of the spectral quantum efficiency of the photocathode.

In the experimental studies conducted, the detection efficiency could be characterized for the visible spectrum between 460 nm - 650 nm. The detection efficiency continuously decreases from $\sim 20\,\%$ at 460 nm for larger wavelengths, approaching $0\,\%$ towards the cut-off wavelength of the photocathode material of around 700 nm. The temperature dependence of the DE in the UV-spectrum could not be investigated in the framework of this thesis, since it was failed to comply to upper and lower limits in the intensity, necessary to obtain unbiased results for gain and DE.
It would be of high interest to tackle the challenges faced, since the typical wavelengths for the operation in IceCube is typically in the UV-range up to the blue end of the visible spectrum. It is likely that the experimental methods can be adjusted to comply with the intensity limits by adjusting the attenuation for wavelength ranges, where the intensity exceeded the boundaries.

The effect of temperature in the range of $-40\,^{\circ}$C - $20\,^{\circ}$C however, is subordinate to the spectral dependence for the visible spectrum. To quantify the impact of cooling across the observed spectrum, two temperature coefficients were introduced, which linearly approximate the in- or decrease in absolute DE $\beta_{\mathrm{DE}}(\lambda)$ or relative DE compared to room temperature $\alpha_{\mathrm{DE}}(\lambda)$, due to changes in temperature.

The investigation of the coefficients showed, that temperature can have an enhancing or weakening effect on the detection efficiency, depending on the wavelength of the incident light. Approaching the blue end of the visible spectrum between 460 nm - 520 nm, where the detection efficiency is the highest for the observed spectrum, an increase of DE as a consequence of cooling could be observed. The highest increase in this region could be observed at 510 nm, where the DE increases by cooling by $0.015\,\%\,^{\circ}$C^{-1}. For the in-ice temperature variations for IceCube Upgrade, for the spectrum between 460 nm - 520 nm, thus differences of below $\sim 0.15\,\%$ in detection efficiency can be expected. As the DE characteristics varies from PMT to PMT, differences of several percents in DE are common for the blue end of the spectrum [10, p. 71]. Since these differences are much larger than the temperature effects on the DE, the temperature dependence is likely to be insignificant for IceCube Upgrade.

A notable feature in the relative temperature dependence to room temperature, is that the relative detection efficiency significantly drops for decreasing temperatures, approaching the red end of the spectrum. At 650 nm, the relative DE increases with $0.7\,\%\,^{\circ}$C^{-1}. Similar rises have been observed for bialkali [25] and other photocathode types [26, p. 246]. This might

be related to the low absolute DE towards the red region of the spectrum, accompanied by a rise in dark rate due to an increase of thermionic emission. Thermionic emission leads to the detection of electrons, that have not been released by the photoelectric effect, which falsely results in measurement of a higher DE. Similar characteristics from previous studies have observed similar increases [25].

Further studies could explore the following aspects in greater depth:

- Locating the origin of the systematic shift in gain that appeared using the setup for the UV spectrum. Exploring the temperature dependence in the UV region down to $350\,\mathrm{nm}$ would expand the characterization of the temperature dependence of DE for the mDOM PMT to the most relevant spectrum for IceCube.

- Investigating the material-dependent nature of the temperature dependence of bialkali photocathodes. Comparing measurement results with theoretical approaches as such as Spicer's three-step model has the potential to understand the nature of the characteristics in a more profound way.

This thesis showed that the temperature dependence of the DE for the investigated spectrum is likely to be negligible for the operation of the Hamamatsu R15458-02-Type PMTs in the framework of IceCube Upgrade, which potentially negates the necessity of temperature-specific modifications for the detector models.

Furthermore, the studies emphasized the complexity of the temperature dependence of bialkali PMTs for temperatures between $-40\,^{\circ}\mathrm{C}$ - $20\,^{\circ}\mathrm{C}$, enabled by the high spectral resolution in the visible spectrum, which possibly revealed local extrema, which were not observed in previous research.

A Appendix

A.1 Limits of Charge Spectrum Fitting

The charge spectra of the PMT response are fitted based on equation 3.4.6. As the equation contains up to eight free fitting parameters, fitting the charge spectrum requires cautious preparation of the free parameter space and initial guesses. As the intensity of the incident light rises, accurate fitting of the spectrum becomes more inaccurate, since the localization of the pedestal and modelling of the convolution of the charge contributions becomes successively harder.
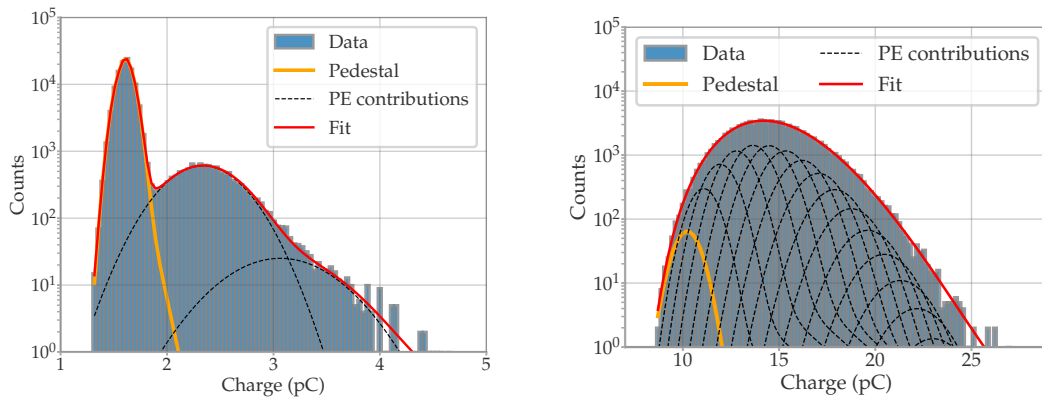
FIGURE A.1.1: **Left:** Fit of the charge spectrum for $\mu \approx 0.1$. **Right:** Attempt to fit a charge spectrum for $\mu \approx 5.2$.

As seen in the left figure of fig. A.1.1, for low light intensities, the charge spectrum is dominated by the contribution of the pedestal, while the charge contributions is largely made up out of contributions of 1 PE and 2 PE events. As the mean number of the incident photons is highly increased as seen in the right subplot, where the mean number of photoelectrons reaching the multiplication system μ is approximately 50 times higher than in the left subplot, the fit is dominated by multi-PE contributions. The resulting convolution is usually hard to trace back to the many Gaussian contributions it is made of. In [10, p. 54] it was observed that the charge fit is not affected from changes in light intensity if $0.1 < \mu < 1$ (SPE). For higher intensities of $\mu \gtrsim 2$, experience shows that systematic distortions are to be expected, including for Q_1.

A.2 Consequences of Stacking Reflective Neutral Density Filters

In the setup for the investigation of the wavelength and temperature dependence of the DE, a combination of two **reflective** ND-filters was used, as described in section 4.2.1. The transmittance of the ND-filters was measured beforehand, to obtain the spectral transmissivity of
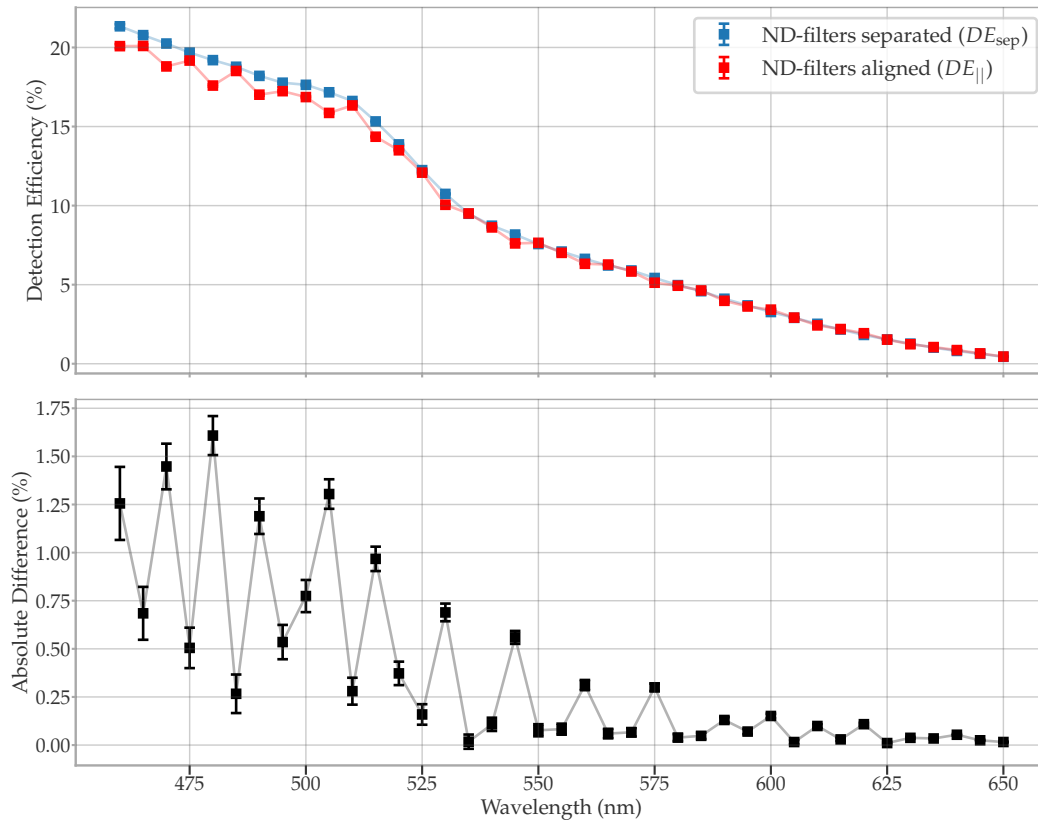
FIGURE A.2.1: The upper plot shows the measured detection efficiencies for aligning the reflective ND-filters in parallel right behind each other (red) and separating them with the fiber in between (blue). The absolute value of the difference of the two datasets is shown below. Note that both figures share the same x-axis. The connecting lines are purely meant for better visualization and do not represent measured data. Some uncertainties are smaller than the used markersize.

the specific filters in use. However, the transmittance of the combination could not be measured, since the combined attenuation of two filters with optical densities of 2.0 and 3.0 is too high to transmit a measurable number of photons to the photodiode for the used light source. Thus, the transmittivities of the ND-filters were measured separately. It was assumed that the optical densities are additive, when combined in a beam path. As the measurements for the investigation of the wavelength and temperature dependence of DE were conducted, unexpected kinks were noticed in the blue end of the spectral response (red, fig. A.2.1), appearing for the same wavelengths for all observed temperature steps, different to the characteristics presented in [10]. This led to the conclusion that there might be a systematical error in the optical setup. Finally, the source of the systematic could be identified as the assumption, that the ND-filters do not interact with each other when placed in succession in the beam path. This could be concluded, by measuring the detection efficiency as previously (see fig. 4.2.1), but separating both ND-filters, so that one is located in the climate chamber in front of the PMT, while the other one stays in the same position as before. The obtained detection efficiency DE_{sep} is shown in fig. A.2.1, and compared to the previous results, where the ND-filters were aligned in parallel right behind each other $DE_{||}$ (from fig. 4.2.7). As seen in the upper plot of fig. A.2.1, the systematic kinks for the blue end of the spectrum disappear, when the filters are separated by the optical fiber in between them. The magnitude of the systematic error is shown in the lower plot as the absolute value of the difference in between both measurements $|DE_{||} - DE_{sep}|$. Apparently, that systematic error generally increases for lower wavelengths, while it fluctuates with rising amplitude around this trend approaching lower wavelengths.
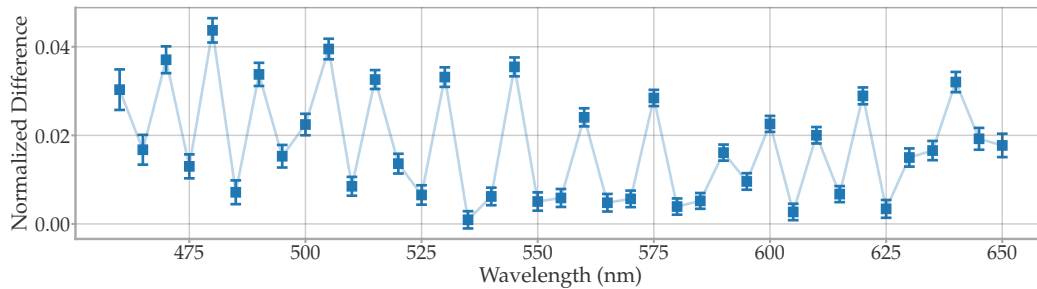
FIGURE A.2.2: Normalized difference of the two measurements with different ND-filter positioning. The connecting lines are purely meant for better visualization and do not represent measured data.

However, looking at the normalized difference of both measurements as

$$\frac{|\mathrm{DE}_{||} - \mathrm{DE}_{\mathrm{sep}}|}{|\mathrm{DE}_{||} + \mathrm{DE}_{\mathrm{sep}}|},\qquad\text{(A.2.1)}$$

the systematic error is not higher for lower wavelengths intrinsically, but increases for a higher detection efficiency (see fig. A.2.2). It is likely that the systematic is the consequence of multi-reflections between the filters, which would increase N_λ and thus decrease the detection efficiency. Nevertheless, since this systematic error does not distort the temperature dependence characteristics of the detection efficiency, the previous measurements were used for further discussion in this thesis.

A.3   Wavelength-Dependence of the Transit Time

For the setting of the charge integration window, an approximation of an expected transit time helps to fully capture each waveform, whilst keeping the integration window as small as possible, to prevent systematic errors due to correlated background. Thus, the transit time for each wavelength was determined by measuring the time of the maximum of the voltage drop for 10^5 waveforms and performing Gaussian fits on the histogram of the measured values subsequently. The mean value of the fit is then selected as the center of the charge integration window. As can be seen in fig. A.3.1, the transit time continuously decreases for higher wavelengths. The upper end for the transit times lies at $202.24(92)\,\mathrm{ns}$ for $460\,\mathrm{nm}$ and the lower end at $202.82(75)\,\mathrm{ns}$ for $650\,\mathrm{nm}$. Thus, as the maximal differ-
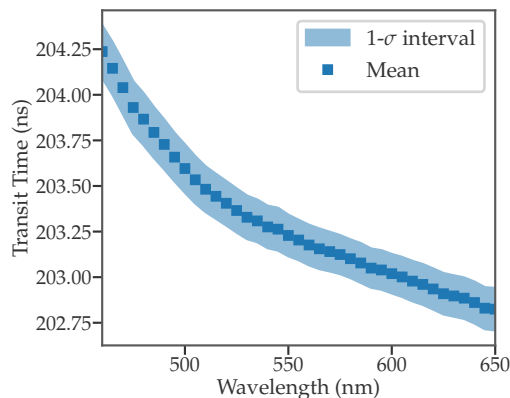

FIGURE A.3.1: Mean transit times, determined by fitting the transit time histogram for each wavelength step with a Gaussian. The standard deviations are displayed as a continuous region for better visualization.

ence in transit time over the spectrum of $1.41(18)\,\mathrm{ns}$ is very small compared to the charge integration window size of $\pm 30\,\mathrm{ns}$, the wavelength-dependence of the transit time, due to higher initial velocities of the photoelectrons, is rather negligible. Nevertheless, the determined spectral transit times were used to set the charge integration window.

Bibliography

[1] IceCube Collaboration. *IceCube Neutrino Observatory - Detector*. Accessed: 2024-05-25. URL: https://icecube.wisc.edu/science/icecube/.

[2] E Andres. "The AMANDA neutrino telescope: principle of operation and first results". In: *Astroparticle Physics* 13.1 (Mar. 2000), 1–20. ISSN: 0927-6505. DOI: 10.1016/s0927-6505(99)00092-4. URL: http://dx.doi.org/10.1016/S0927-6505(99)00092-4.

[3] IceCube Collaboration. *IceCube Neutrino Observatory - Research Highlights*. Accessed: 2024-06-24. URL: https://icecube.wisc.edu/science/research/.

[4] Aya Ishihara. *The IceCube Upgrade – Design and Science Goals*. 2019. arXiv: 1908.09441.

[5] IceCube Collaboration. *IceCube Neutrino Observatory - Cosmic Ray Physics*. Accessed: 2024-09-13. URL: https://icecube.wisc.edu/science/research/#cosmicrayphysics.

[6] Wolfgang Pauli. "Pauli letter collection: letter to Lise Meitner". Typed copy. URL: https://cds.cern.ch/record/83282.

[7] J. A. Formaggio and G. P. Zeller. "From eV to EeV: Neutrino Cross Sections Across Energy Scales". In: *Rev. Mod. Phys.* 84 (2012), pp. 1307–1341. DOI: 10.1103/RevModPhys.84.1307. arXiv: 1305.7513 [hep-ex].

[8] R. Abbasi et al. "Measurement of the high-energy all-flavor neutrino-nucleon cross section with IceCube". In: *Physical Review D* 104.2 (July 2021). ISSN: 2470-0029. DOI: 10.1103/physrevd.104.022001. URL: http://dx.doi.org/10.1103/PhysRevD.104.022001.

[9] R. E. JENNINGS. "ČERENKOV RADIATION". In: *Science Progress (1933-)* 50.199 (1962), pp. 364–375. ISSN: 00368504, 20477163. URL: http://www.jstor.org/stable/43425324 (visited on 05/14/2024).

[10] M. A. Unland Elorrieta. *Development, simulation, and characterisation of a novel multi-PMT optical module for IceCube Upgrade with emphasis on detailed understanding of photomultiplier performance parameters*. Zenodo. 2023. DOI: 10.5281/zenodo.8121321. URL: https://doi.org/10.5281/zenodo.8121321.

[11] M.G. Aartsen et al. "Measurement of South Pole ice transparency with the IceCube LED calibration system". In: *Nuclear Instruments and Methods in Physics Research Section A: Accelerators, Spectrometers, Detectors and Associated Equipment* 711 (May 2013), 73–89. ISSN: 0168-9002. DOI: 10.1016/j.nima.2013.01.054. URL: http://dx.doi.org/10.1016/j.nima.2013.01.054.

[12] IceCube Collaboration. *IceCube Neutrino Observatory - Galery*. Accessed: 2024-06-24. URL: https://icecube.wisc.edu/gallery/.

[13] T. Anderson et al. *Design and performance of the multi-PMT optical module for IceCube Upgrade*. 2021. arXiv: 2107.11383.

[14] P. Buford Price et al. "Temperature profile for glacial ice at the South Pole: Implications for life in a nearby subglacial lake". In: *Proceedings of the National Academy of Sciences* 99.12 (2002), pp. 7844–7847. DOI: `10.1073/pnas.082238999`. eprint: `https://www.pnas.org/doi/pdf/10.1073/pnas.082238999`. URL: `https://www.pnas.org/doi/abs/10.1073/pnas.082238999`.

[15] A. G. Wright. *The Photomultiplier Handbook*. Oxford University Press, June 2017. ISBN: 9780199565092. DOI: `10.1093/oso/9780199565092.001.0001`. URL: `https://doi.org/10.1093/oso/9780199565092.001.0001`.

[16] A. Einstein. "Über einen die Erzeugung und Verwandlung des Lichtes betreffenden heuristischen Gesichtspunkt". In: *Annalen der Physik* 17 (1905). [17 pp.] (EAP, 164; CPE 2, 149), pp. 132–148. URL: `https://myweb.rz.uni-augsburg.de/~eckern/adp/history/einstein-papers/1905_17_132-148.pdf`.

[17] H.M. Araujo et al. "Study of bialkali photocathodes below room temperature in the UV/VUV region". In: *IEEE Transactions on Nuclear Science* 45.3 (1998), pp. 542–549. DOI: `10.1109/23.682445`.

[18] Lew Classen. "The mDOM–a multi-PMT digital optical module for the IceCube-Gen2 neutrino telescope". PhD thesis. FAU Erlangen-Nürnberg, 2017. URL: `https://www.uni-muenster.de/imperia/md/content/physik_kp/agkappes/abschlussarbeiten/doktorarbeiten/1702-phd_lclassen.pdf`.

[19] E.H. Bellamy et al. "Absolute calibration and monitoring of a spectrometric channel using a photomultiplier". In: *Nuclear Instruments and Methods in Physics Research Section A: Accelerators, Spectrometers, Detectors and Associated Equipment* 339.3 (1994), pp. 468–476. ISSN: 0168-9002. DOI: `https://doi.org/10.1016/0168-9002(94)90183-X`. URL: `https://www.sciencedirect.com/science/article/pii/016890029490183X`.

[20] L. Kuballa. *Untersuchungen zur Ausgabelinearität von Photomultipliern des Typs Hamamatsu R12199-02 sowie des Einflusses des Erdmagnetfelds auf die Photomultiplier-Eigenschaften*. Bachelor Thesis. 2017. URL: `https://www.uni-muenster.de/imperia/md/content/physik_kp/agkappes/abschlussarbeiten/bachelorarbeiten/1710-ba_lkuballa.pdf`.

[21] Norbert Wydra. "Studien zur Temperaturabhängigkeit der Quanteneffizienz eines Photomultipliers vom Typ Hamamatsu R12199-02". Bachelor Thesis. 2018. URL: `https://www.uni-muenster.de/imperia/md/content/physik_kp/agkappes/abschlussarbeiten/bachelorarbeiten/bachelor_thesis_wydra.pdf`.

[22] Inc. Thorlabs. *Mounted UV Fused Silica Reflective ND Filters*. `https://www.thorlabs.com/newgrouppage9.cfm?objectgroup_id=3193&pn=NDUV502A`. Accessed: 2024-09-17. 2024.

[23] A.J. Dekker. "Secondary Electron Emission". In: *Advances in Research and Applications*. Ed. by Frederick Seitz and David Turnbull. Vol. 6. Solid State Physics. Academic Press, 1958, pp. 251–311. DOI: `https://doi.org/10.1016/S0081-1947(08)60728-6`. URL: `https://www.sciencedirect.com/science/article/pii/S0081194708607286`.

[24] M.A. Unland Elorrieta et al. "Characterisation of the Hamamatsu R12199-01 HA MOD photomultiplier tube for low temperature applications". In: *Journal of Instrumentation* 14.03 (Mar. 2019), P03015. DOI: `10.1088/1748-0221/14/03/P03015`. URL: `https://dx.doi.org/10.1088/1748-0221/14/03/P03015`.

[25] A. S. Singh and A. G. Wright. "The Determination of Photomultiplier Temperature Coefficients for Gain and Spectral Sensitivity Using the Photon Counting Technique". In: *IEEE Transactions on Nuclear Science* 34.1 (1987), pp. 434–437. DOI: `10.1109/TNS.1987.4337379`.

[26] Hamamatsu Photonics K.K. *Photomultiplier Tubes - Basics and Applications*. 4th. Japan: Hamamatsu Photonics K.K., 2017. URL: `https://www.hamamatsu.com/content/dam/hamamatsu-photonics/sites/documents/99_SALES_LIBRARY/etd/PMT_handbook_v4E.pdf`.

[27] Raffaela Solveig Busse. "Setup and commissioning of a test stand for detailed investigations of quantum efficiency characteristics of photomultiplier tubes, and initial studies for IceCube-Gen2". Master's Thesis. Universität Münster, 2017. URL: `https://www.uni-muenster.de/imperia/md/content/physik_kp/agkappes/abschlussarbeiten/masterarbeiten/1703-ma_rbusse.pdf`.

[28] W.E. Spicer and Alberto Herrera-Gomez. "Modern theory and application of photocathodes". In: *Proc. SPIE* 2022 (Jan. 1993), pp. 18–33. URL: `https://cds.cern.ch/record/257133/files/P00020029.pdf`.

[29] Willem Achtermann. "Replication of a photomultiplier in COMSOL Multiphysics® to study PMT performance parameters for the mDOM in IceCube". Accessed: 2024-09-25. Master's Thesis. Universität Münster, 2024. URL: `https://www.uni-muenster.de/imperia/md/content/physik_kp/agkappes/abschlussarbeiten/masterarbeiten/masterarbeit_willem_achtermann.pdf`.

[30] Alissa Puke. "Modellierung und Untersuchung der Sekundärelektronenemission in einem Photomultiplier mit COMSOL Multiphysics". Unpublished Bachelor's Thesis, forthcoming. 2024.

[31] Fynn Peters. "Studien zur Wellenlängenabhängigkeit von Performance Parametern von Photomultipliern des Typs Hamamatsu R12199-01HA". Bachelor Thesis. Universität Münster, 2020. URL: `https://www.uni-muenster.de/imperia/md/content/physik_kp/agkappes/abschlussarbeiten/bachelorarbeiten/ba_fpeters.pdf`.

Acknowledgements

Declaration of Academic Integrity

I hereby confirm that this thesis on the "Studies on the Temperature Characteristics of the Detection Efficiency of Hamamatsu R15458-02-Type Photomultipliers" is solely my own work and that I have used no sources or aids other than the ones stated. All passages in my thesis for which other sources, including electronic media, have been used, be it direct quotes or content references, have been acknowledged as such and the sources cited.

Signature:
_____

Date:
_____

I agree to have my thesis checked in order to rule out potential similarities with other works, and to have my thesis stored in a database for this purpose.

Signature:
_____

Date:
_____